Enhancing the Simultaneous Alignment and Sorting of Carbon Nanotubes by

Sunmeng Wang

A thesis
presented to the University of Waterloo
in fulfillment of the
thesis requirement for the degree of
Master of Science
in
Chemistry (Nanotechnology)

Waterloo, Ontario, Canada, 2020

Author's Declaration

I hereby declare that I am the sole author of this thesis. This is a true copy of the thesis, including any required final revisions, as accepted by my examiners.

I understand that my thesis may be made electronically available to the public.

Abstract

Carbon nanotubes have broken through the barriers of our imagination and are currently being investigated for various nano-electronic device applications. Successful implementation in these applications however, often requires strict control of their properties and orientation. As such, post-synthesis processing must be performed prior to any device fabrication. These processing techniques often aim to either address the challenges associated with sorting and alignment individually. A novel method called the alignment relay technique aims to address both of these issues simultaneously. As the introduction of this process was merely a proof of concept, focus must be put in place to enhance the performance and efficacy. In an attempt to improve this technique, we alter the temperature, liquid crystal, iptycene design as well as means of alignment as attempts to accomplish this. At the same time, mechanistic details are revealed to gain a better insight of the nanoscopic dynamics.

Preparation of preliminary materials and apparatuses are initially performed. We first build a Polarized Optical Microsope (POM) in order to observe the liquid crystal dynamics. Despite its frequent use in a research setting, the cost can be upwards of thousands of dollars. As only qualitative observations are required, we decided to build our own model. In this section, we provide a blueprint for the construction of an economical POM with a heating stage and digital connection for facile recording of data, totaling about \$150-\$200. We subsequently demonstrate its effective application in visualizing liquid crystals. After the microscope is made, various molecules are synthesized to gain the chemical resources needed for the alignment. In an attempt to circumvent some of the hazards asssociated with the original synthesis, an alternate route to create iptycene (**5**) is first explored. Despite having success in the initial parts of the synthetic sequence, an inability to replicate literature conditions causes the final step to produce only a 2% yield. Thus, we are forced to abandon this procedure and revert to using the original route to making the molecule. A smaller iptycene molecule (**9**) is subsequently made through attaching the anchoring group directly to one of the intermediates appearing in the synthesis of iptycene (**5**). Finally, a separate liquid crystal (**11**) is synthesized through two nucleophilic additions with 4-hydroxy-4-biphenylcarboxylic acid. These materials provide us the necessary grounding to perform experiments with the alignment relay technique.

After the preliminary materials are gathered, the effects of changing the temperature, liquid crystal and iptycene on CNT depositions are observed. An increase in temperature from 25 °C to 70 °C with a nematic liquid crystal (ZLI-1185) do not yield great results as standard deviations are over 45 °. Attempts at using a more ordered smectic A liquid crystal mixture do not aid results either. In fact, we obtain no CNT deposition at all with these

attempts. From this, we gather that controlling both the alignment and functionalization of iptycenes at higher temperatures prove to be a challenging task. As a result of the unknown parameters of both functionalization and alignment kinetics, higher temperature experiments are abandoned. Next, iptycene **(9)** is used to probe the sorting effects of the alignment relay technique. As the size of the cavity on this molecule is significantly smaller in comparison to the original iptycene **(5)** we expect smaller CNT's to be deposited onto the surface. Unfortunately, alignment of this molecule in liquid crystal media is a potential issue due to the smaller size. Consequently, no CNT's are spotted on the surface. Valuable mechanistic insights are obtained from these changes in variables in the alignment relay technique.

Finally, magnetic fields are explored as a viable method for alignment. From these experiments, we find that the performance is positively associated with the magnetic field strength. The standard deviation in alignment between a 0.6 T field and 0.9 T field are 55 º and 24 º respectively with also a clear Gaussian distribution found in the latter condition. Trends for selectivity however, are unconfirmed as Raman spectroscopy using 532 nm and 633 nm lasers show conflicting information. The 532 nm laser show the best selectivity under a 0.9 T field while the 633 nm laser suggested that the 0.6 T has the better selectivity. Despite needing further data to establish a pattern between field strength selectivity, general patterns remain congruent with previous reports as the same diameter CNT's (1.44 nm and 1.59 nm) are present on the substrate surface. These positive results allow the use of magnetic fields to be the basis of future alignment experiments and processes. Benefits as a result of this change include limiting exposure of the substrate to dust, adjustable alignment and reusability.

Acknowledgements

These past two years were easily some of the most arduous in my life. Errors, failures and faulty judgement were among a few of the recurring themes during this period. Despite this insanity, an odd sense of tranquility appeared every now and then. I credit this to the strong sense of camaraderie built by a community of like minded individuals who are struggling through the same experience. No matter where I went or who I talked to, the actions people bring in this community are of nothing but support and encouragement. I wish to give special thanks to Rafael, Jianan, Serxho, Sara + Sarah, Geoff, Parisa, Monika and everyone else in the Schipper group for taking this seemingly endless ride with me. Of course, this statement is generously extended to Dr. Derek Schipper who was more than just a mentor and supervisor. In addition, I would like to thank my parents as they have been the greatest motivating factor and reminding me to never give up.

Table of Contents

List of Figures

List of Tables

Nomenclature

POM Polarized Optical Microscope, page 11

ppb   parts per billion, page 8

ppm parts per million, page 52

RBM Radial Breathing Mode, page 31

s   singlet, page 52

sc   semiconducting, page 7

SSRI Selective Serotonin Reuptake Inhibitor, page 2

t   triplet, page 52

ZLI-1185 4'-Pentyl-bicyclohexyl-4-carbonitrile, page 23

Chapter 1

Introduction

1.1 Organic Chemistry

Organic chemistry consists of manipulating structures derived from the upper right sector of the periodic table, revolving around carbon. Historically, organic chemistry has yielded many useful innovations in the fields of medicine and consumer plastics.

In the field of medicine, the development of antidepressants added another dimensionality to our previous hypotheses of depression and gave a better insight into the human psyche. Among a few theories for the cause of depression in the early 20th century, are Sigmund Freud's theory of objective loss (i.e. death of a loved one or romantic breakup) and Viktor Frankl's theory of a lack of personal meaning (i.e. the presence of an existential vacuum).[1,2] From these hypotheses, humanistic approaches such as logotherapy emerged, which emphasized the pursuit of silver linings in times of adversity.[3] Meanwhile, in the realm of practical neuroscience, lobotomies and electric shock therapies were becoming commonplace to tackle this enigmatic disorder. Previous approaches of understanding and treating depression came from humanistic avenues or from top down approaches.[4] It was only in the 1950's that a possible biochemical explanation for depression came to light when doctors noted strange side effects from patients taking the drug, Isoniazid (Figure 1.1). Isoniazid was initially a drug used to treat tuberculosis, however, it was noted that some users experienced an increased feeling of well-being and increased appetite.[5] This lead to further exploration for the drug but unfortunately, inconsistent results from various independent doctors prevented this lead from taking off.[6] Despite the poor results, the method of modifying internal biochemistry became a route that many researchers began taking seriously as
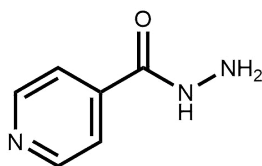
Figure 1.1: Chemical structure of Isoniazid

drugs specifically targeting the treatment of depression began to materialize.[7-10] The rest is history as this subsequently inspired studies to explore the influences of neurotransmitters on mood, which then paved way for the development of drug classes like selective serotonin reuptake inhibitors (SSRI's) and mono-amine oxidase inhibitors (MAOI's). With the development of better and more complex molecules, some important neurological pathways implicated during the pathology of depression were soon elucidated.[11,12] Thus, without organic chemistry, our understanding of the biochemical contribution to the human psyche would be insufficient.

Polymers are widely abundant in biological matter. Glycogen acts as an energy storage medium in the muscles.[13] Cellulose acts as a protective barrier and as a source of rigidification for plants.[14] Deoxyribonucleic acid (DNA) is the basis for the genetic coding of life. For living organisms, enzymes catalyze these reactions allowing a wide variety of these biochemical materials to be easily manufactured within the confines of their own cells. Manipulating matter outside of this realm to make polymers however, proved to be challenging. One of the first synthetic polymers was introduced only in 1907, when the Belgian-American chemist, Leo Baekeland exploited the condensation between phenol and formaldehyde to make Bakelite. This polymer would be commercialized in plethora of consumer products from radios to firearms.[15]

Despite the introduction of synthetic polymers in the early 1900's, what they were and the mechanism by which they were formed remained relatively unknown until the late 1920's. This was when Harvard researcher Wallace H. Carothers began his publications about polycondensation and its comparison to polyaddition. Most importantly, he outlined that polymers were high molecular weight species and not special aggregates of smaller molecules. From this, came simultaneously his initial publications on synthesizing polyester, which would be widely adopted today in clothing and various forms of packaging.[16] In 2016, polyester dominated the global fiber trade, owning over 55% of the total market share.[17] Polycondensation proved to be the basis of many futuristic materials at the time. Applying this principle to monomers with multiple aromatic components, yields high performance

polymers such as aramids (aromatic polyamides). One of the most notable examples in this class being Kevlar, which possesses high structural rigidity, flame-tolerance and overall toughness per unit area. These qualities make this material suitable for bulletproof vests, tires and ropes.[18]
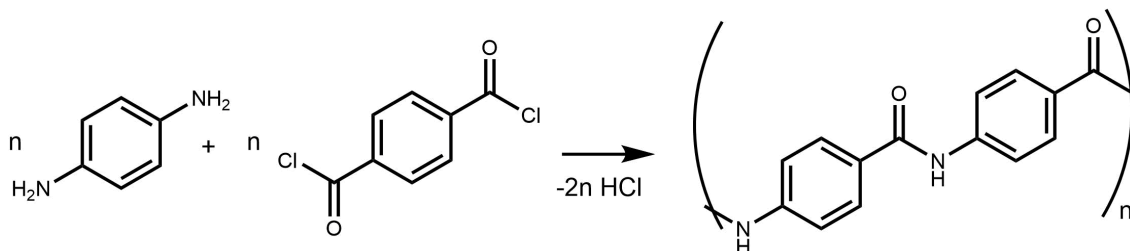
Figure 1.2: Synthesis of Kevlar through polycondensation

The polymer industry would face another wave of momentum moving into the 21st century when advancements in organometallic chemistry yielded, what were otherwise, impossible transformations.[19] Stille and Suzuki couplings, for example, allowed for facile formation of biaryl motifs through direct C-C bond formation. As a result, extended conjugated systems could be made, thus providing steam to the field of conjugated polymers.[20] These materials would be implemented in OLED (organic light emitting diodes) , solar and thin film transistor technologies.[21] Palladium catalyzed transformations did not simply stop here however. Direct arylation carried this torch forward by improving efficiencies of material synthesis in various fronts, enhancing synthetic control and doing this all in an eco-friendly fashion. An example of this would be the enhancement in the synthesis of poly(3-alkylthiophene)s (P3AT) .[21] Prior to direct arylation, one of the methods to make P3AT's was through the oxidative coupling of alkyl thiophenes via the $FeCl_3$ catalyst. These reactions had maximum yields in the 50% range due to uncontrollable regioselectivity during the polymerization process, forming head-head, head-tail and tail-tail species (Figure 1.2).[22-24] Direct arylation, like its predecessors, only stitches together specifically activated regions, thus allowing regioselectivity to be tightly controlled. As a result, it is not uncommon for desired P3AT's to be synthesized with yields of 99%.[25,26] Thus, not only has palladium cross coupling given birth to countless new materials, it has also been able to increase the efficiency in the ability to mass produce pre-existing ones. Thus, consumer products like plastic packaging and displays have all benefited in some way shape or form due to developments in organic chemistry.

3
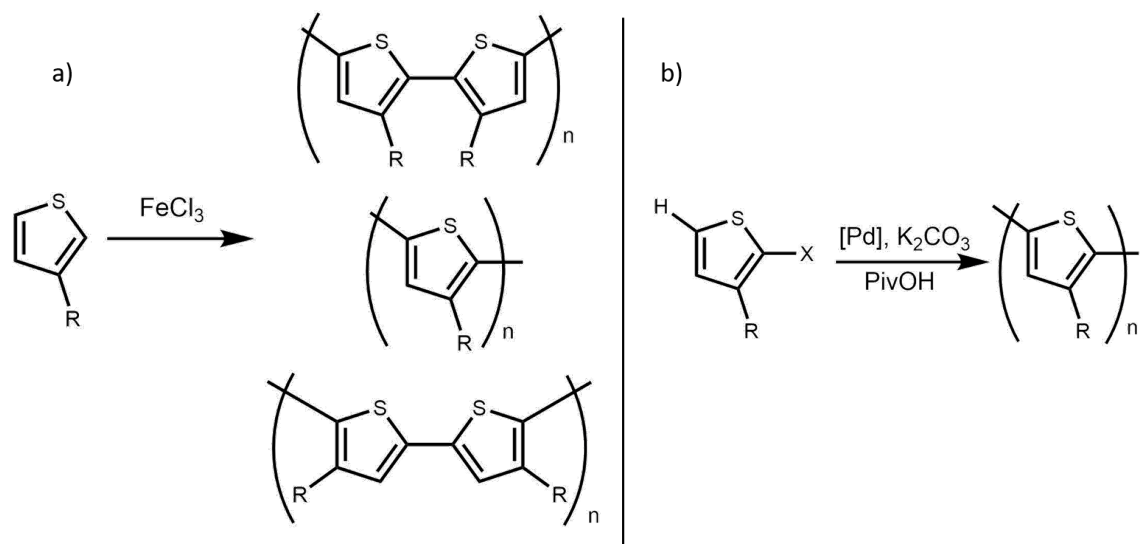
Figure 1.3: a) Head to head, head to tail and tail to tail polymer formation of P3AT with oxidative polymerization b) Controlled head to tail regioselectivity via direct arylation polymerization

Organic chemistry prove to be a powerful catalyst to continuously usher improvements to our health and leisure. Our goal is to continue this trend and use these molecules to help us innovate in the realm of nanotechnology.

1.2 Nanotechnology

Nanotechnology focuses on the very small and has many grandiose goals. Some of which include: perfecting the construction of the basic building blocks of various forms of matter, elucidating their unique properties, integrating them into technological applications and the ability to preserve and replicate the nanoscopic features of promising candidates to the commercial scale. This field has experienced an exponential boon in the past decade. In fact, according to a recent report by StatNano, the number of nanotechnology research publications increased from 19,754 in the year 2000 to 141,663 in 2015.[27] Whether it is finding a way to create monodisperse conjugated polymers to enhance uniformity in optoelectronic properties, or finding the perfect mixture of components for a new composite, our newly developed thirst for understanding the world of the small contains great promises of ushering the world into a new era of technology and innovation.

4

One area that has caught a lot of attention is the field of thin films. Thin film electronic materials have a wide variety of applications including touch screens,[28] solar cells,[29] flexible circuits[30] and implantable biological sensors.[31] Technological evolution over time in this area has made it possible to precipitate new features, increase performance or decrease the cost of production to adapt to consumer demands. One example for which this has happened is the introduction of OLED's. This technology has allowed for the production of astonishingly thin displays previously inaccessible by liquid crystal display (LCD) technology while simultaneously improving other features such as viewing angle and response time.[32,33] The culmination of these desirable traits in a commercial product lead to the successful development of a market worth an expected \$30.3 billion in 2019.[34] Another example for which technological innovation has accommodated to changing economic demands is the development of perovskite solar cells. Global energy consumption is expected to increase by 28% from 2015 to 2040.[35] At the same time, the vast supply of technology from tractors to smartphones across the globe has caused an accelerated rate of carbon dioxide emissions.[36,37] As a result, perovskite solar cells have emerged as an energy resource to tackle the economic and environmental burdens faced by the world. It is emerging as the fastest improving solar technology ever realized with power conversion efficiencies reaching over 20% in the latest improvements.[38,39] Furthermore, their facile means of production coupled with its flexibility is congruent with the current theme of portability and convenience in today's market. Technological evolution in various thin film products has taken part in the drastic change of people's lives with bigger disruptions incoming for the future.

The emergence of new nanomaterials has created an attractive niche for the field of optoelectronics. Carbon nanotubes (CNT's), quantum dots and perovskites are among some of the contenders for the next generation of sensors and thin film devices. CNT's possess a slew of attractive physical and electrical properties, as well as stability making it a highly competitive option in this broad ecosystem. Among some of CNT's physical attributes are their high Young's modulus (450 Gigapascals (GPa))[40] and high decomposition temperature (525 °C) for dense, vertically aligned films.[41] In the following segments, we will discuss the attractive electronic properties of CNT's in various device settings.

1.3   Carbon Nanotubes

CNT's can be conceptualized as a sheet of graphene rolled into a cylindrical tube. Atoms comprising the lattice structure are characterized as being approximately sp^2 hybrids

throughout. The pristine surface and geometry of carbon nanotubes makes these materials difficult to solubilize. As a result, there are always impurities or imperfections added for successful dispersion in solution. Surfactants like sodium deoxycholate and various polymers are typically used as a non-invasive means of enhancing the solubility of this material. The pristine structure can also be partially disrupted in order to add functional groups that enhance solubility.[42,43] This is often done by adding CNT's to H_2SO_4 or HNO_3 to carboxylate the surface, improving its dispersive ability in aqueous solutions.[44,45] Unfortunately, this covalent functionalization also deteriorates optoelectronic properties.[46] Thus, the addition of elements to solvate this material is viewed as a necessary evil at this point in time.
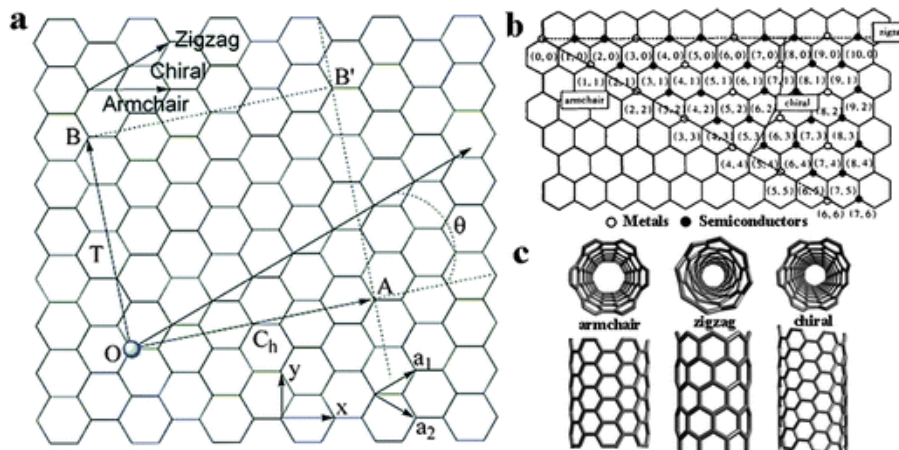
Figure 1.4: (a) Schematic plot of the chiral vector (Ch) in a graphene 2-D lattice. (b) The relationship between integers (n,m) and the metallic or semiconducting nature of nanotubes. (c) The structure of "armchair", "zigzag" and "chiral" nanotubes. [47]

CNT's exist in many different structures: they can be single walled, double walled or multi-walled.[48] For the purpose of this project, we will be focusing on single walled carbon nanotubes (SWCNT's). SWCNT's can be geometrically identified with a set of two dimensional indices, m and n. These values correspond to the exact manner by which it is theoretically folded from an origin on graphene and is illustrated in Figure 1.4. These indices are important as different folds produce CNT's of different diameters and chiralities, leading to variations in electronic properties.[49-51] As a general rule, if the difference between m and n is equally divisible by three, the CNT behaves like a metal, whereas all other scenarios yield semiconducting behavior. Further, it can be said that the bandgap scales inversely proportional to the diameter of the CNT.[52-54]

The perfection in lattice structure of this material gives rise to unparalleled thermal and conductive properties. Some of which include: ballistic transport,[52,55,56] low power consumption,[57,58] high tensile strength[40,59,60] and exceptional stability.[61,62] To further highlight some of these attributes, we will walk through some application examples.

1.3.1 Field Effect Transistors

Field effect transistors (FET's) are high performance electrical switches used in computer processors. CNT's possess ideal characteristics to make the functionality of existing FET's even better. Figure 1.5 provides a visual of these novel CNTFET's. Electronically, CNT's possess quasi-ballistic transport, providing faster charge transport, while at the same time, reducing the energy emission in the form of phonons.[63-65] A recent demonstration evaluating the performance of a 10 nm CNTFET showed an operational voltage of 0.4 V, in comparison to 0.7 V by a state of the art 14 nm metal oxide semiconductor field effect transistor (MOSFET) normalized for a CNT density of 125 $CNT/\mu m^2$.[66] On/Off current ratios indicate how well the device can distinguish a signal between its on and off state. High On/Off ratios of 1 x 10^8 have been reported for individual devices,[67] while a ratio of 1 x 10^7 was attained for a network.[57] Despite demonstrating excellent properties, some of these qualities can only be maintained for homogeneously aligned and sorted batches of CNT's. In contrast, the carrier mobility can be up to 40 times lower in a random network.[68,69] Whereas, On/Off ratios can be decreased by up to three orders of magnitude if there is even a 1% increase in metallic CNT content.[70] Thus, CNT's have incredulous properties that are suitable for FET applications but must overcome fundamental challenges of sorting and alignment for widespread adoption.

1.3.2 Solar Cells

Due to the semiconducting (sc) nature of CNT's, it is only natural to evaluate the use of this as a light harvesting material. There are many different solar cell architectures based off of CNT's. The most promising of which has been the hybrid CNT/Si solar cells, reaching efficiencies of 17% for p-CNT and 4% for n-CNT.[72] The manufacturing process of these carbon nanotube solar cells can play a huge role in dictating the efficiency of these devices. Firstly, purity of the material used is an important consideration as increasing the purity of the sc-CNT's from 95% to 97% nearly doubles the efficiency of a solar cell.[72] Secondly, vertical alignment is crucial for the fabrication of this technology as the CNT's doubles
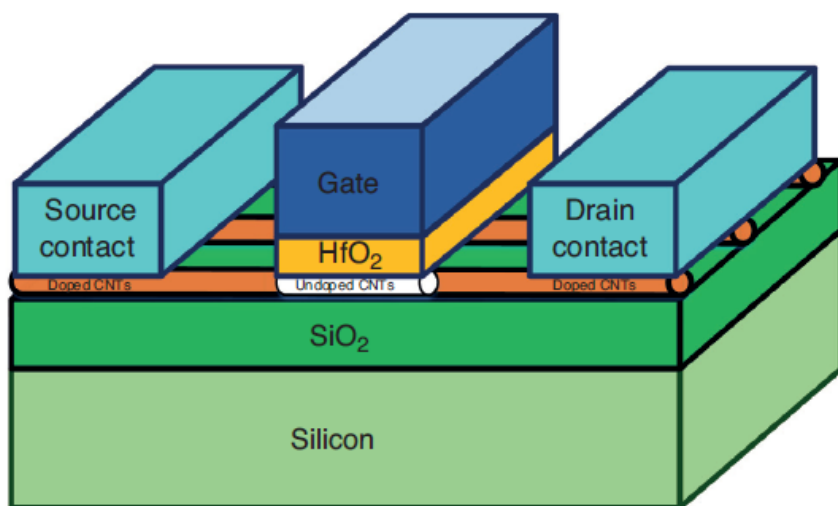
Figure 1.5: CNTFET Modelled After a Traditional MOSFET[71]

as a surface passivation layer to prevent recombination.[74] Thus, while the performance for carbon nanotube based solar cells lags behind some of the other options like perovskites, efforts to improve the purity and alignment will ultimately yield better efficiencies.

1.3.3   Sensors

CNT's exhibit the ideal geometric and electronic qualities for sensor applications. Due to the one-dimensional nature of the material consisting of only surface atoms, any molecular adsorbate will cause a perturbation to its resting electronic state.[58,75] Not only this, specifically, CNT's have an unusually high affinity for gasses like NO_2 and NH_3. In fact, Li et al. demonstrated a CNT sensor with a detection limit of 44 parts per billion (ppb) for NH_3.[76] Chemical modifications can further be done on CNT's to improve detection limits and to sense other chemical species. In 2003, Qi et. al. built a similar sensor to the one from Li et al, except, the CNT's were coated with polyethylenimine.[77] The result was a device in which the detection limit for NH_3 was lowered to 1 ppb. To sense other chemical species, CNT's functionalized with the amino acid, cysteine, were able to detect Pb^{2+} and Cu^{2+} at levels of 1 ppb and 15 ppb respectively.[78] Much like the previous cases, CNT's must also be sorted and aligned for high performance sensor assemblies. Unsorted, aligned networks of CNT's exhibit a dramatic decrease in response signals.[79] Thus, as the evolution of technology progresses into the future, CNT's are highly likely to play a significant role

in our ever-changing atmosphere.

1.3.4   Production and Processing

Significant effort has been made in an attempt to bring these next generation electronic devices to life. Unfortunately, numerous challenges still exist regarding their production and processing, preventing the materialization of CNT based devices. Recall that different CNT's have different electronic properties; any minor deviation on this nanoscopic scale will carry forward to the macroscopic. Therefore, to extract the maximum potential of CNT based devices, we would ideally need to consistently produce monodisperse batches in-situ or from ex-situ processing.

Methods aimed at addressing the sorting issue include using rationally designed nanoparticles for CVD growth and ex-situ sorting methods like voltage breakdown and ultracentrifugation. A CVD chamber consists of an inlet for feeding in reactant gases, an outlet for removing exhaust and a tube furnace for pyrolysis. Its operation involves controllably pyrolizing the reactant gases being fed into the chamber to yield product structures on a substrate surface. In the case of CNT formation, the reactant gases consists of hydrogen (reducing agent) and various forms of carbon (e.g. ethanol) diluted by an inert carrier gas such as helium or argon. To enhance the yields for CNT production, metal catalysts are used to as general pyrolysis can yield plethora of different allotropes like fullerenes and amorphous carbon. Specific catalysts like cobalt and nickel can further control CNT nucleation and dictate CNT chirality as a result of varying contact energies between the catalyst and each CNT chirality.[54,80] It is important to note however, that state of the art technology can only realize a 57% yield for synthesizing SWCNT's of a single chirality and 99% yield for synthesizing general SWCNT's with most processes yielding outcomes far worse than that.[81,82] Results are highly dependent on many factors. Some of which include: the purity of reactants used, catalyst lifetime, substrate quality (purity and topography). The preparation required to produce high quality results is both intensive and expensive. As a result, research focusing on the qualitative separation of CNT's post-growth is also an important undertaking in today's time. Voltage breakdown is a low cost method to separate CNT mixtures. This method involves patterning a transistor design around a CNT sample. The semiconducting CNT's are turned to their "off state" by applying a positive gate bias. This is as a result of the intrinsic p-type nature of the CNT under an oxygen rich environment (otherwise, it would be negative for n-type). An electrical pulse is then passed through the source and the drain. This causes the electron carriers in the sample

(especially from the conductive metallic CNT's) to excite and generate a lot of heat. This heat concentrates generally in the middle of the CNT and promotes an oxidation process that effectively destroys the channel of the CNT. As a result, metallic CNT's, they are removed, leaving pure semiconducting CNT's behind. The benefit of this method is that this purification step can be built on top of the device manufacturing process, saving time and effort. Unfortunately, if further separation of semiconducting CNT's is needed, then another method must be consulted as the separating CNT's of different band remains a challenge with voltage breakdown.[83-85] Ultra-centrifugation is another promising technique which involves wrapping the CNT's in surfactant mixtures, then subjecting the samples to centrifugation at speeds of 40,000 RPM+.[86] The principle behind this is that upon interacting with the surfactant mixture, the CNT's would possess different buoyancies which can be exploited via centrifugation. This technique has been demonstrated to separate CNT's of different sizes even directly from a wide mixture of carbon allotropes.[87] Unfortunately, much like the CVD method, cost is an issue and as a result, this method is difficult to scale. Due to challenges that many examples for sorting face for large scale applications, sorting is still an important task being investigated in various stages of CNT procurement.

Another major challenge associated with producing CNT devices is alignment. High quality devices cannot be patterned onto CNT's directly as most techniques used for mass production result in randomly oriented bundles. As such, CNT's must be delineated into organized arrays to expose their unique properties. It has been shown that organized arrays results in carrier mobility differences of up to 40 times while the on/off ratio can be an entire order of magnitude off.[88-89] Current methods of alignment include dry shearing,[90] gas flow,[59] filtration[91,92] and magnetic fields. Dry shearing uses an aligner and uses frictional force to shear a thin film of CNT deposited on the surface of a substrate.[90] The results are dependent on the size of the CNT with performance being inversely proportional to diameter. This method is non-invasive meaning that it will not negatively alter the properties of the raw material. However, this also means that it will not be able to positively affect the sample either. Contaminants that are found in the original sample like residual catalysts are spotted on scattered electron micrographs. Thus, this method requires that starting materials be relatively pure. Slow filtration is another non-invasive alignment technique in which an aqueous CNT suspension is filtered through a porous membrane. Results, as always when handling various forms of nanomaterials, are dependent on a variety of stringent factors. In this case, these factors include surfactant choice, surfactant concentration, CNT concentration and speed of filtration and CNT production method. Controlling every one of these parameters yield the possibility of achieving crystalline levels of alignment across a wide domain in which the range of Gaussian distributions are within +/- 5 °.[92,93] Finally, we can take things back to the CVD chamber and control the inlet gas flow amongst

10

other parameters to dictate alignment directly during the germination process. Mechanistic studies have shown that short CNT's are unable to interact with the gas flow as well as long CNT's. Thus, This focus yields only long but uniformly aligned CNT's.[94,95] Commercialization of this is again, yet to be realized as CNT's must be grown on expensive substrates such as quartz or sapphire and require laborious preparation.[64, 96-98]

1.4 Alignment Relay Technique

As sorting and alignment processes are often independent, it can be an inconvenience to perform each process separately. One unique approach of processing CNT's is to address both of these challenges simultaneously.[99] The Alignment Relay Technique (ART) developed by the Schipper group is an example of that. It involves a rubbed polyimide alignment layer passing information onto a layer of liquid crystal. The liquid crystal then passes this information onto iptycene molecules. These molecules finally pass both this as well as sorting information onto CNT's, thus completing the relay. The following paragraphs describe the main components involved in this process.

1.4.1 Liquid Crystals

Liquid crystals are compounds that possess physical states exhibiting qualities of both the solids and liquids. The solid-like qualities manifest as areas of orientational and positional order, forming domains that can be seen on a polarized optical microscope (POM) . The liquid-like properties come in the form of mobility as molecules are not completely fixed in a solid lattice.[100] Combining various degrees of positional and orientational orders yield the different mesophases that liquid crystals can exhibit; these include the nematic state and smectic states. The nematic phase is defined as having orientational order but lacking positional order (Figure 1.6a). Thus, thread like defects can be seen as a result disclinations within ordered domains.[101] The smectic phases are found at temperatures lower than the nematic and can be separated into many sub-phases. They possess both orientational and positional order.

Liquid crystals in both the nematic and smectic phases possess the unique attribute to be able to undergo uniaxial alignment with an alignment interface. One method is through the use of a physically rubbed alignment layer. When subjected to this interface, liquid crystal molecules on the surface interact with the trenched arrays and relays the alignment

information through the bulk of the medium. Figure 1.6b demonstrates alignment through a physical interface.[102-104] Other forms of alignment include the using electric and magnetic fields. Liquid crystals have electric dipoles in which one end is partially positive and the other, partially negative. This contrasting feature allows them to align with electric field flux, with the degree proportional to liquid crystal's electric susceptibility. Further, as a consequence of the electric charge separation, there is a dynamic circulation of electrons between the two dipoles which subsequently creates a perpendicular magnetic field. This allows the medium to interact with magnetic field flux with the degree proportional to the liquid crystal's magnetic susceptibility.[105-108]
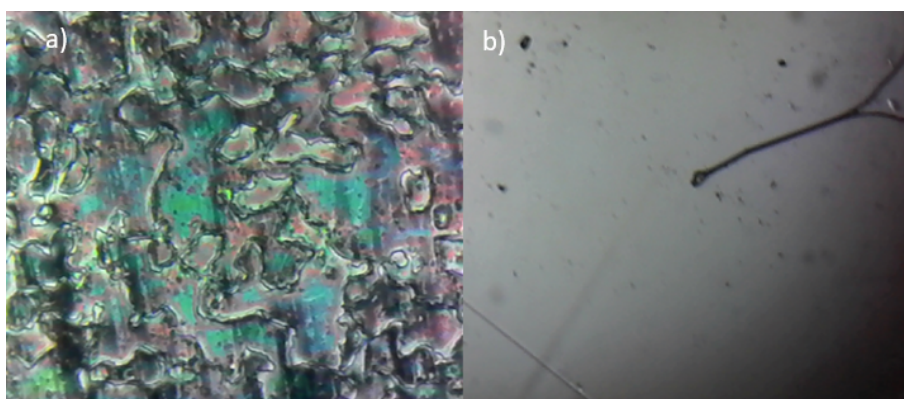
Figure 1.6: a) Nematic phase of liquid crystal exhibiting colorful patterns called Schlieren lines b) Same sample in the smectic A phase that has undergone uniaxial alignment under a magnetic field

1.4.2   Iptycenes

Iptycenes are a general class of organic compounds characterized by fused arenes bonded to a barellene centre. A few physical characteristics of this class of compound include good thermal stability, rigidity and large pockets formed between the "arms".[109] An interesting aspect of these molecules is that liquid crystals are able to interact with the structure and minimize the free space created by the "arms". As a result, they have the possibility to orient the molecules depending on how the liquid crystals are aligned (Figure 1.7b).[110] As a molecule with many localized areas of aromaticity, the π system throughout can participate in π-π interactions like many similar systems. In fact, their curved structure allows them to interact with the π system in CNT's and can provide a scaffold for which they can be

bound to (Figure 1.7c).[111] This is the basis of the selection principle as iptycenes with varying degrees of concavities and sizes would preferentially bind to CNT's of a given size.
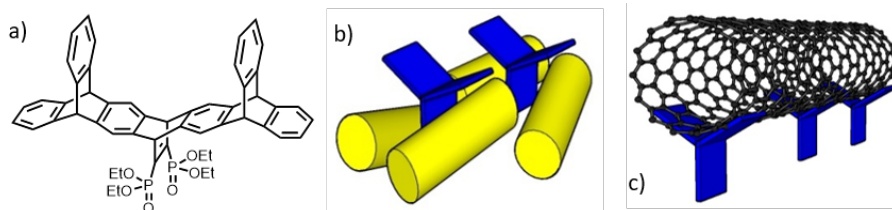
Figure 1.7: a) Example iptycene structure b) Minimization of free space by liquid crystals c) Illustration of accumulated π stacking from iptycene arrays

1.4.3 Anchoring Groups

Referring back to what was said previously, the iptycenes follow suite of the liquid crystal undergoing uniaxial alignment. However, this configuration is not solidified as any perturbation to the system will destroy its orientation. As such, the molecules need to be anchored onto the the substrate surface in order to set the desired orientation in place. This can be done by attaching anchoring groups on the molecule. One preliminary requirement for this group is that it must form multiple bonds in order to prevent rotation of the iptycene after functionalization. As this requirement is mostly design related, multiple options are available at our disposal. One example is to use silane groups. Silanes readily form covalent bonds on surfaces like silicon dioxide, alumina and titanium dioxide.[112] Unfortunately this group is not practical as installation is quite tedious on our iptycene system. Another example at our disposal are thiols. This group however, forms strong bonds only with gold interfaces.[113] Given these additional constraints, the best candidate we have at our disposal are phosphonate esters. They readily form rigid covalent bonds on a wide variety of metal and metalloid oxide surfaces such as silicon oxide and indium tin oxide.[114-116] The groups are relatively easy to install through a Diels Alder attachment. There has also been precedence of using this element in an optoelectronic setting further reinforcing its adoption.[117] Figure 1.8 illustrates how these anchoring groups attach to the surface.
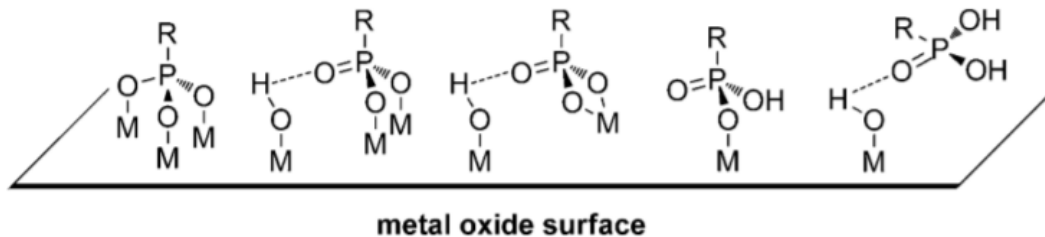
Figure 1.8: Attachment configurations of phosphonate esters to metal oxide surfaces[112]

1.4.4   Assembly

The Alignment Relay Technique for sorting and aligning CNT's is illustrated in Figure 1.9 and goes as follows:

1. A mixture of liquid crystal and iptycene is made and a drop of the mixture is sandwiched in between a silicon shard and a polyimide alignment substrate. As the liquid crystal aligns with the rubbed polyimide film, so will the iptycene molecules through the minimization of free space.

2. The mixture is left for 24 hours for the iptycene molecule to chemisorb onto the silicon surface via condensation.[118]

3. Finally, the excess mixture is washed off with solvent and the silicon shard is immersed in a carbon nanotube solution. CNT's would only bind to areas with a high abundance of π- πinteraction.

4. Excess CNT's are washed off with MilliQ water and samples are analyzed via atomic force microscopy (AFM) and Raman spectroscopy.

14
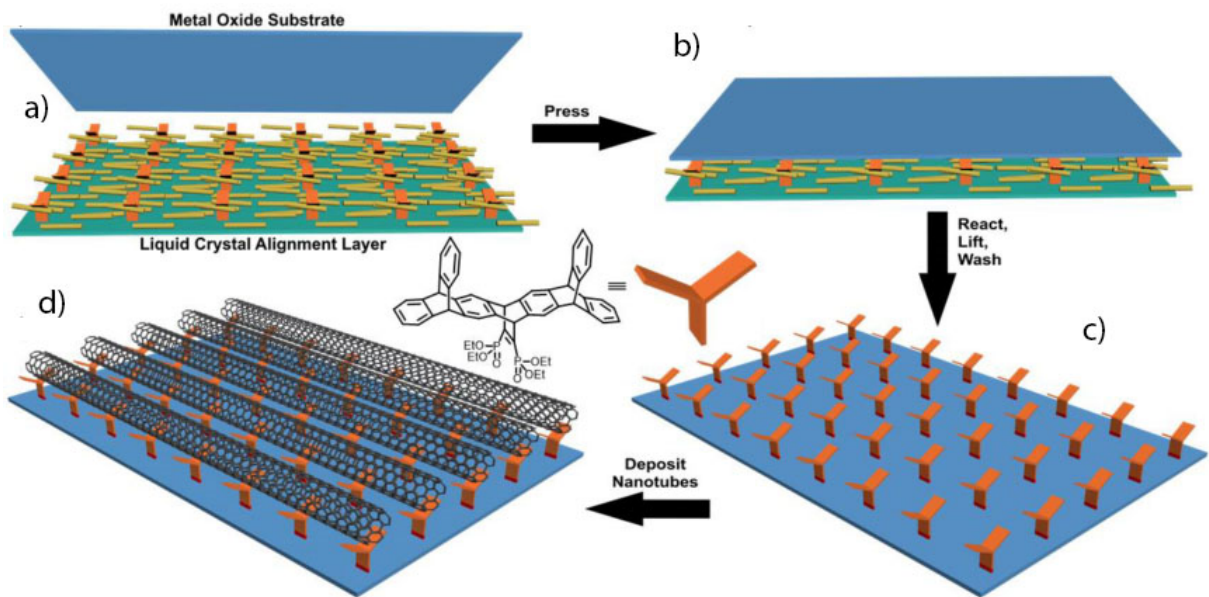
Figure 1.9: ART schematic for aligning and sorting SWCNT's[99]

Instead of requiring separate processes to sort and align CNT's, the ART provides a powerful framework to simultaneously perform both steps. The tools needed to implement this process are low-cost and readily available. Further, results so far have been obtained solely from performing the process on a chemistry lab bench-top without needing to enter a clean room. A synopsis of these results include Gaussian distributed alignment histograms as well as a clear demonstration of selective CNT removal. The versatile nature of the ART demonstrates not only the ability to control alignment and sorting but attributes like length as well.[99,126,134] This unorthodox selection feature could yield unexpected benefits in the realm of device manufacturing in the future as this sets a uniform channel length for transistor manufacturing. The advantages of using the ART for CNT processing is clear. However, adjustment still needs to be made in order to optimize results. Limitations that this process currently face include low CNT density, non-uniform alignment and a lack of precedence demonstrating adjustable diameter sorting results. The process would also benefit from additional modifications to further enhance economic viability. In the following correspondence, we discuss attempts to address these limitations by modifying the temperature used for functionalization, changing the liquid crystal, altering the iptycene design and replacing the disposable alignment layers with a magnetic alignment apparatus.

15

Chapter 2

Results and Discussion

2.1   Low Cost Polarized Optical Microscope

2.1.1   Construction

A POM was first constructed to aid in the analysis of some liquid crystal mixtures.

The microscope setup was constructed using a Plugable USB microscope, purchased from Amazon, capable of 250x magnification (Figure 2.1a). The microscope came with a clear plastic housing (Figure 2.1b) that protrudes out from the end with the lens preventing focus of a 250x magnification. To make use of the full magnification, the protruding plastic was first ground off with a dremel tool and then sanded so the maximum focal plane can be easily accessed (Figure 2.1c). Next, a piece of aluminum was milled into a stage using an end mill following dimensions found in Figure A.17. Next, polarized filters were affixed to both the microscope (Figure 2.1c) and stage. The filters employed were obtained from a pair of movie theatre 3D glasses. The starting orientation of the filters must be orthogonal and this was ensured by putting two filters on top of one another first to see which relative position provided a maximum destructive wave interference as indicated by a darkening of the light passing through. It is important to note that not all 3D movie glasses might work as some may use circular polarizing filters instead of linear filters. Thus, it is important to perform this task to also determine if the correct type of filter is in the glasses. Upon distinguishing the correct orientation for the filters, one filter was glued onto the end of the microscope and the other was put into the carved 13 mm well in the stand. Dimensons for this stand can be found in Figure A.8. Finally, an LED circuit was built with the following materials: breadboard, light emitting diode, copper wires, and a 10kΩ resistor. The wiring

of the circuit can be depicted in Figure 2.1e with the schematic diagram found in Figure A.19. The LED was suspended through the 3 mm hole in the stand with the fitting being snug enough for the LED to hold its own weight. If desired, the 10kΩ resistor can be replaced with a 20kΩ potentiometer to add the feature of a tunable light source. The fully assembled apparatus including the computer, microscope, stage, housing and electronics, is shown in Figure 2.1f.
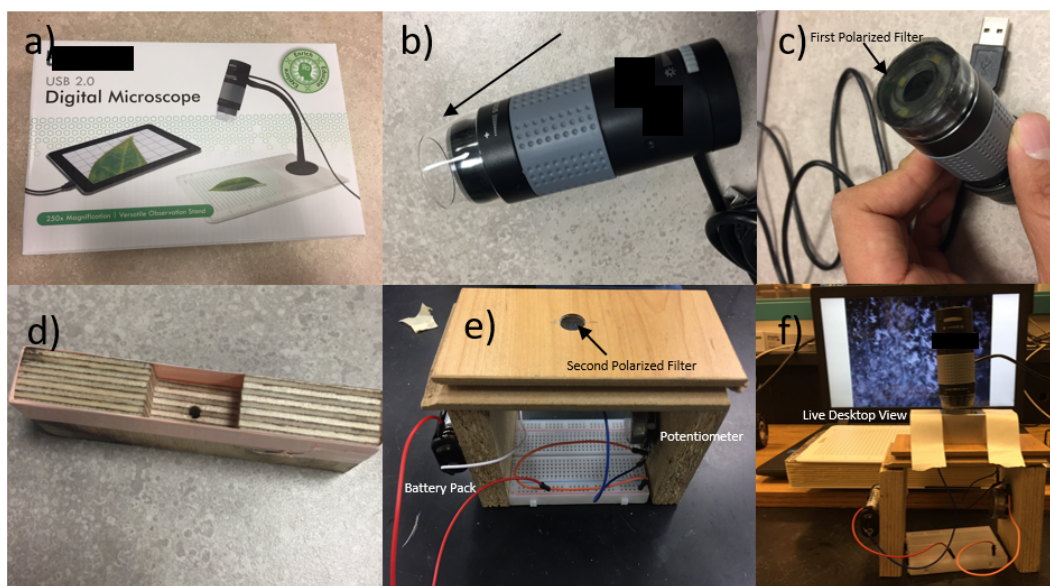
Figure 2.1: a) Commercial Plugable Digital Microscope Kit b) Microscope housing needed to be removed c) Microscope after removing plastic cover and affixing polarized filter d) Teflon wrapped stage e) Stand setup f) Fully assembled apparatus. A milled aluminum stage is shown in this picture instead of a wooden one

2.1.2   Liquid Crystal Observation

Liquid crystals are compounds that exhibit physical states with characteristics of both solids and liquids. For thermotropic examples, these phases can be precipitated by adding or removing heat. These compounds are ideal candidates to be analyzed in a polarized optical microscope as they produce different birefringent characteristics depending on the phase the liquid crystal is in. As a result, a plethora of different images can be seen to evaluate the quality of our setup. Figure 2.2 shows an image taken from the simple microscope setup on a sample of 4-Octyl-4-biphenylcarbonitrile (8CB). 8CB can vary between

a nematic and smectic A liquid crystalline phase depending on the temperature.[119] The image shows 8CB in smectic A phase at room temperature, which is the more organized of the two liquid crystalline states. Visible in the image are randomly orientated grains of liquid crystals giving a "snowy" texture with each grain representing a group of molecules orientated in a particular direction.
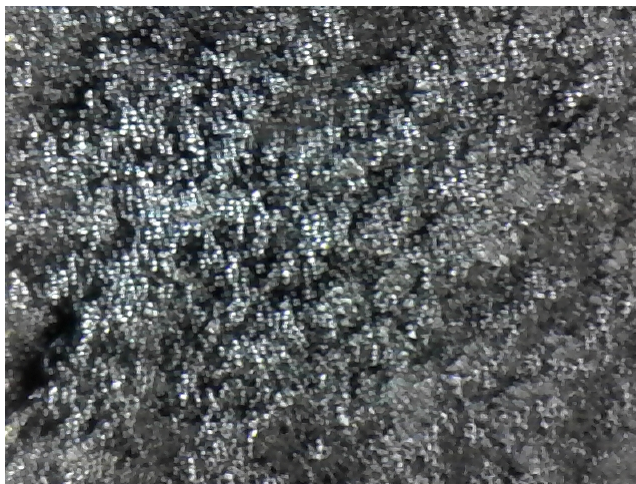
Figure 2.2: 8CB at room temperature in the smectic A phase. This image was directly taken from the low-cost microscope setup

2.1.3   Addition of a Heating Element

The addition of a heating element allows optical properties of thermotropic liquid crystals to be explored. However, as a result of the heating, the polarized filters from the 3D glasses will no longer work as they degrade under high temperatures. Instead, heat resistant polarized filters were purchased from Amazon as a suitable replacement. Under room temperature, 8CB exhibits a smectic A phase, while at 35 °C, it transitions to a nematic phase. Figure 2.3b shows the same 8CB sample from Figure 3 but in the more disordered nematic phase. The nematic state is characterized as having domains with molecules organized in parallel but loses the layered configuration as seen in smectic phase shown in Figure 2.2.[120] This increased disorder is observed macroscopically as a colorful canvas. Microscopically, this can be explained by the different wavelengths of polarized light undergoing numerous refractions and interference patterns through the different organized domains of the material before reaching the microscope.[121]
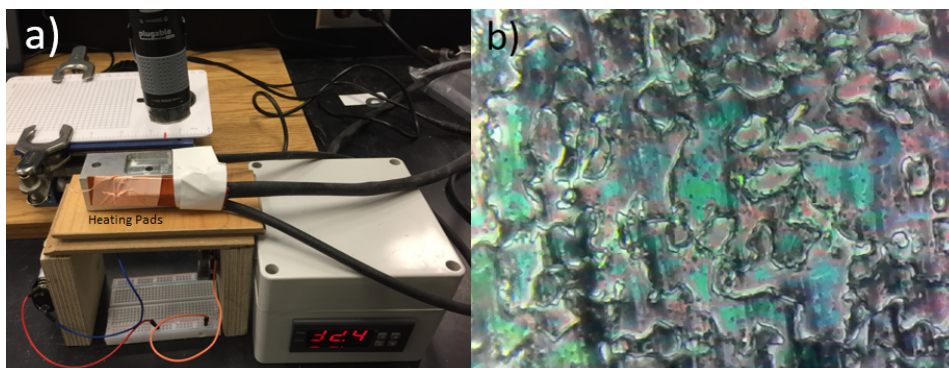
Figure 2.3: Polarized optical microscope setup along with silicon heating pads and aluminum stage b) Nematic 8CB heated to 35 °C. This image was taken directly from the low-cost microscope setup

Our efforts in constructing the POM proved successful and was ready for evaluating the qualities of various liquid crystal mixtures.

2.2   Synthesis

As the ART that was outlined in the introduction was merely a first iteration, there is much room for optimizing the characteristics of the deposited nanotubes like density and selectivity as well as gaining better understanding of the process's underlying mechanics. In order to perform these alterations, we must first gather all the molecules we wish to use. We wish to perform alterations on temperature, liquid crystal and iptycene. Thus, in this section, we outline the procedures that were taken to make two different iptycene molecules along with a liquid crystal that was not available commercially.

2.2.1   Iptycene (5)

Our process began with the synthesis of the iptycene molecule used for the alignment trials. Originally, the synthesis was based off of a procedure from Hart, illustrated in Scheme 1 below.[99]
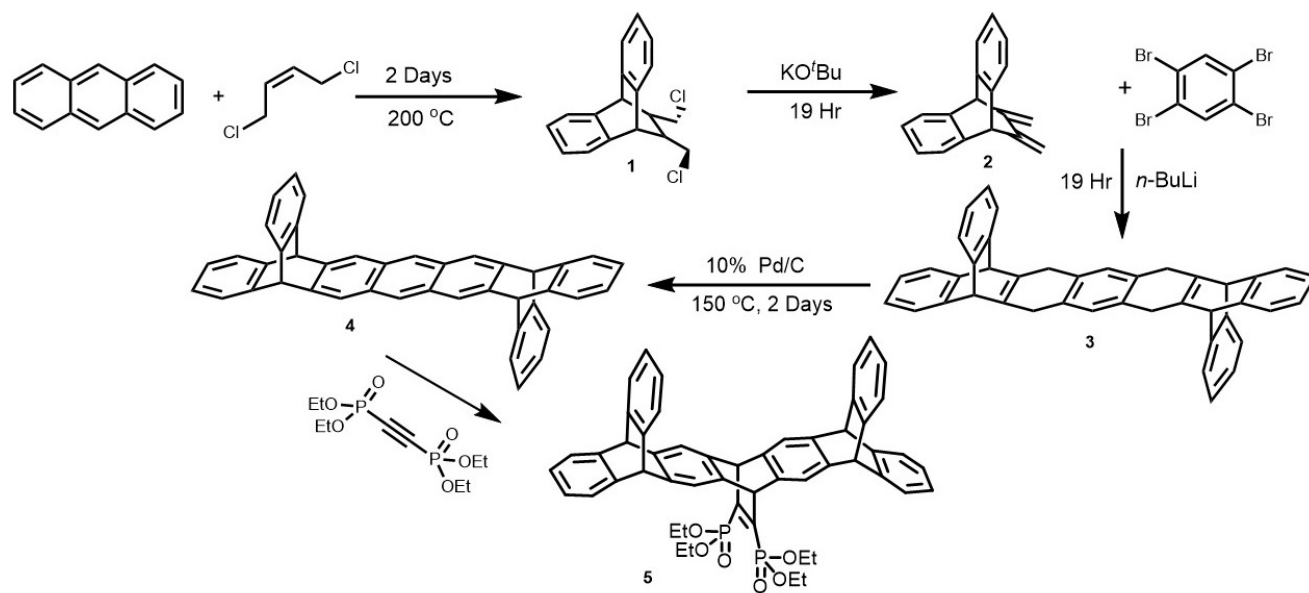
Scheme 1: Synthesis of iptycene (**5**)

In this route, cis-1,4-dichlorobutene was reacted with anthracene at 200 ºC to obtain a Diels Alder adduct in a 65% yield. This adduct was subjected to a double elimination by potassium *t*-butoxide to give the subsequent intermediate in an 80% yield. Another set of Diels Alders were performed with 1,2,4,5-tetrabromobenzene via a benzyne mechanism to yield the general iptycene scaffold in a 58% yield. This scaffold was aromatized with 10% palladium on carbon followed by a final Diels Alder to add the anchoring group to the molecule. NMR spectra for these species can be found in Figures A.1-A.5.

As this method involves the handling of *cis*-1,4-dichlorobutene, an expensive and potent lachrymator under a high pressure environment, an alternative method was investigated to enhance the safety of this process. A literature search showed that (**4**) could be created through another set of Diels Alder reactions followed by a dehydration.[122]. If this process was successful, not only would safety be enhanced but two synthetic steps could also be saved to improve efficiency. Scheme 2 outlines this proposed method.
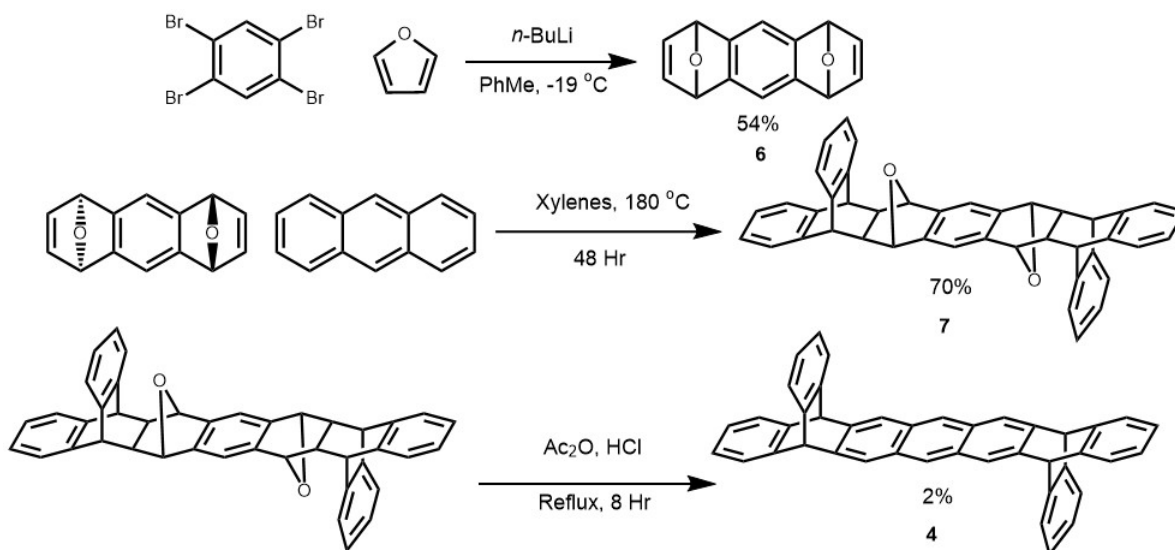
Scheme 2: Synthesis of iptycene molecule (**5**) using an alternate route

Despite successfully reacting furan with 1,2,4,5-tetrabromobenzene to make the diendoxide in a 54% yield followed by another set of Diels Alders with anthracene to yield the following intermediate in a 70% yield, the last dehydration proved to be challenging enough to eliminate this path as a viable alternative for synthesizing our iptycene. It seems that the equipment used could not prevent hydrochloric acid from evaporating out for the duration of the eight hours. Multiple attempts were made to try and contain the acid such as using an ice bucket to cool the water in the condenser and performing the reaction at a lower temperature. Further, transitioning the reaction to a sealed microwave vial yielded a green sludge with no indication of product present. As a result, this method was abandoned and the method illustrated in Scheme 1 was still used to make (**5**) NMR spectra for this set of species can be found in Figures A.6-A.7.

2.2.2 Iptycene (9)

The synthetic route used to make iptycene (**9**) is an offshoot of iptycene 1 and is shown in the figure below:
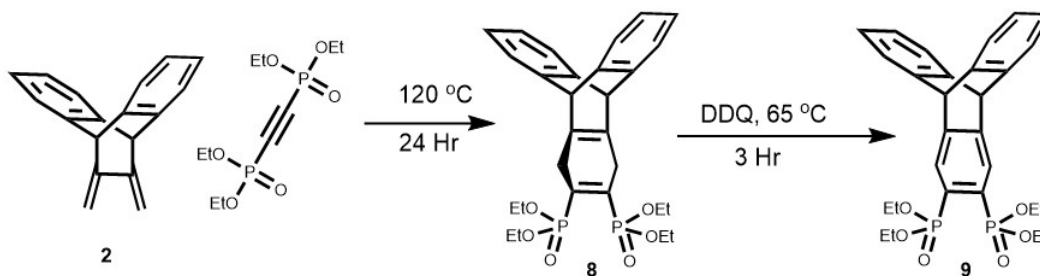
Scheme 4: Synthesis of iptycene molecule (**9**)

In this scheme, intermediate (**2**) from before was directly reacted with the bis(diethoxyphorsphoryl)acetyle to provide the general scaffold in a 50% yield. This was then subjected to 2,3-Dichloro-5,6-dicyano-1,4-benzoquinone (DDQ) oxidation to give iptycene 2 in an 80% yield. NMR spectra for these species can be found in Figures A.8-A.14.

2.2.3 Liquid Crystal (11)

The synthesis of liquid crystal compound (**11**) is laid out in Scheme 3. This process involves a set of nucleophilic additions by 4'-hydroxy-4-biphenylcarboxylic acid. The first nucleophilic addition was to n-bromopentane to yield an intermediate in 48% yield. Subsequently, this product performed a nucleophilic addition to n-bromodecane to give the liquid crystal in an 88% yield. NMR spectra for these species can be found in Figures A.15-A.16.
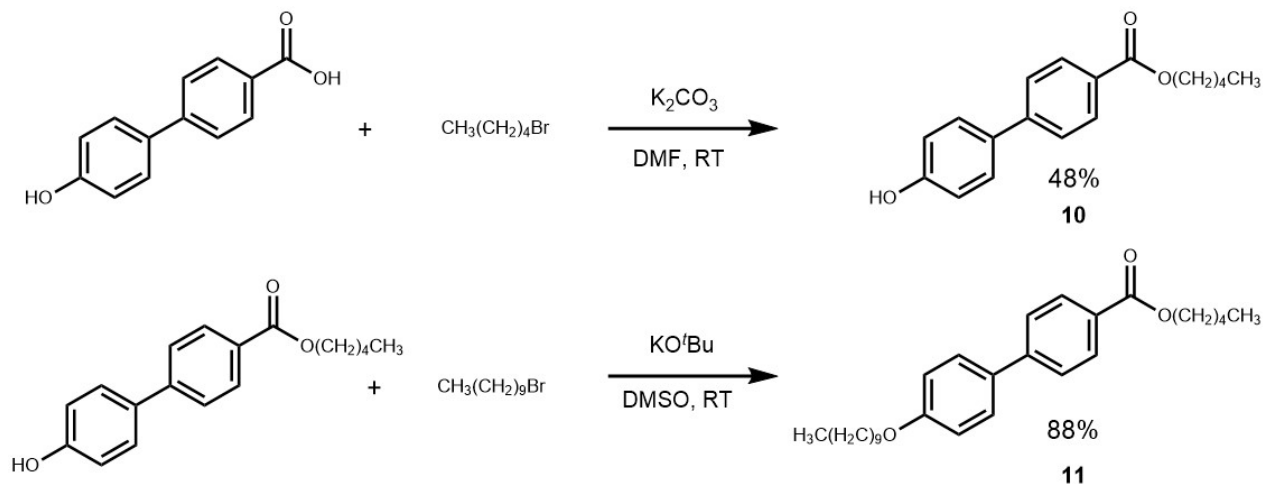
Scheme 3: Synthesis of liquid crystal (**11**)

2.3   Elevated Temperatures for Functionalization

Higher density is required for maximizing the number of devices we can pattern per unit area. We attempt to improve the density compared to previous trials by elevating the temperature for functionalization. The increased rate of reaction would yield molecule deposition to further completion. With more molecule density on the surface, we hope to see an increase in nanotube deposition.

Originally, the functionalization was performed at room temperature while an arbitrary temperature of 70 °C was chosen for functionalization in these trials. To accommodate the change in temperature, another variable in the process must be changed –the liquid crystal. Previously, 8-CB and 4'-pentyl-4-biphenylcarbonitrile (5-CB) were used however, they only exhibit smectic A and nematic phases between 21.5 °C - 40.5 °C and 24 °C - 35 °C respectively.[123] Thus, we must also find a liquid crystal with these phases in the temperature regime we are interested in. 4'-Pentyl-bicyclohexyl-4-carbonitrile (ZLI-1185) exhibits a nematic mesophase between 63.5 °C and 83 °C, making it a suitable candidate for our endeavour.[124] A temperature that avoids the top of that range is picked as the iptycene impurity is added into the liquid crystal, which lowers the transition temperatures.[124]
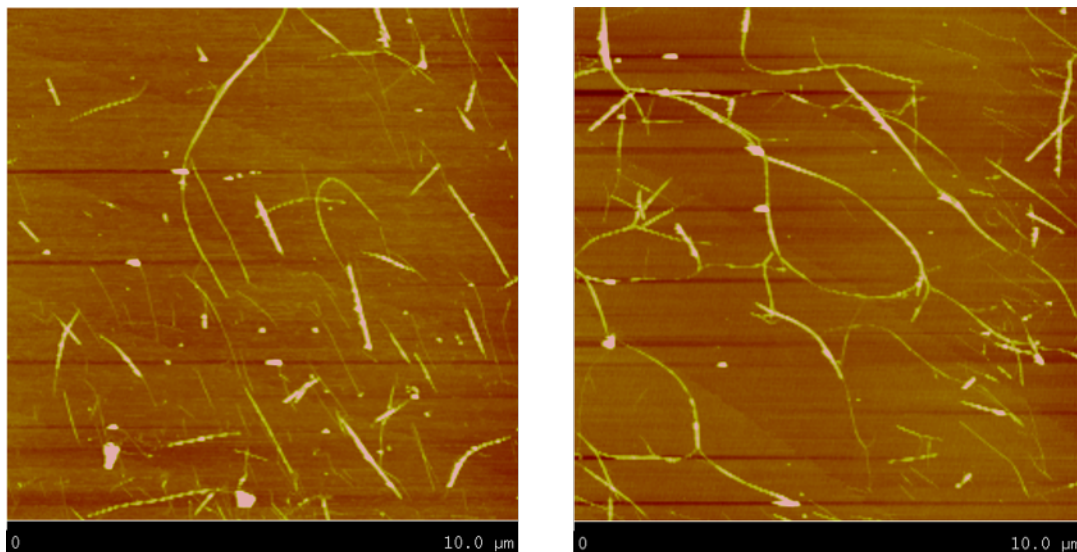

Figure 2.4: AFM images of a silicon shard after ART alignment with ZLI-1185. The full set of images can be found in Figure A.23

23
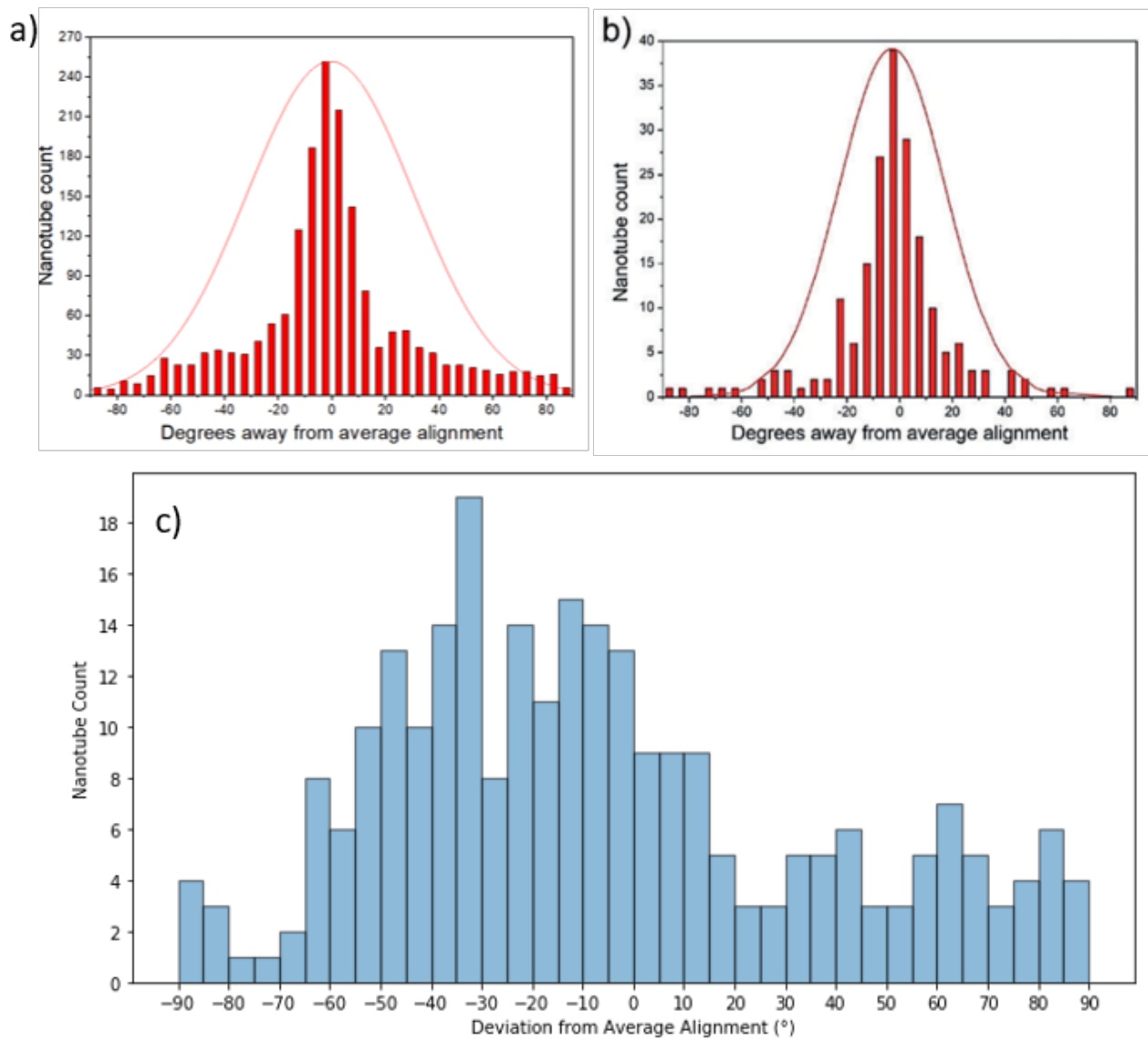
Figure 2.5: a) Angular deviations of individual nanotubes yielded from 8-CB[126] b) Angular deviations of individual nanotubes yielded from 5-CB[99] c) Angular deviations of individual nanotubes yielded from ZLI-1185

24
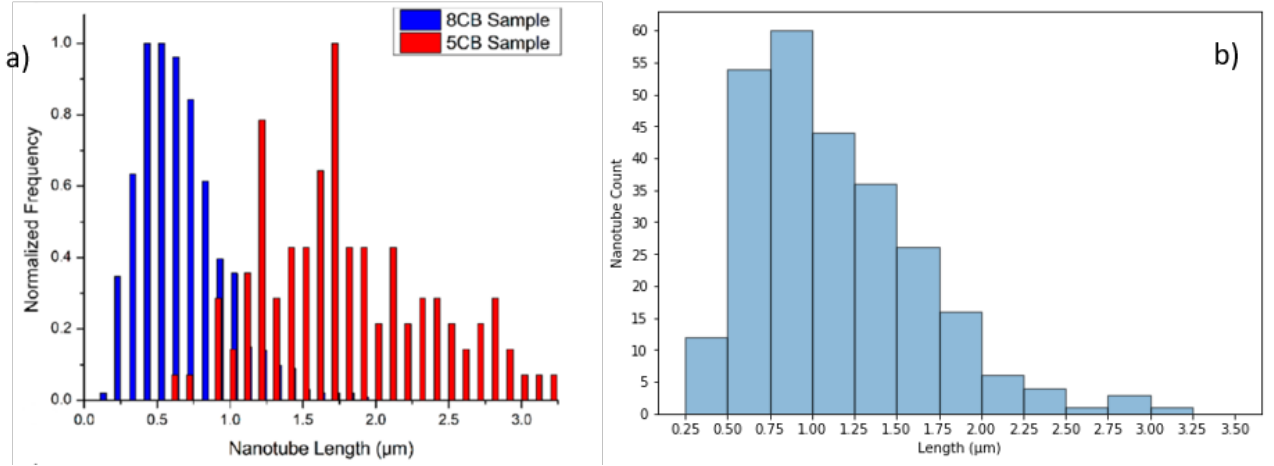
Figure 2.6: a) Length distributions of CNT's obtained using 8-CB and 5-CB[126] b) Length distributions of CNT's obtained using ZLI-1185

The results obtained with ZLI-1185 at an elevated temperature were generally worse compared to both 5-CB and 8-CB trials at room temperature. The density saw an increase from 0.39 CNT/μm^2 to 0.53 μm going from 5-CB to ZLI-1185, however these results still lagged behind those obtained with 8-CB where an average value of 0.81 CNT/μm^2 was obtained. The nature of the liquid crystal could have had an impact in these results as both 5-CB and ZLI-1185 exhibit only nematic phases whereas 8-CB exhibits the more ordered smectic A phase. This would have had an effect on the molecular order of the iptycene molecules which would have relayed imperfections onto the deposited CNT's. Comparing the lengths of CNT's selected between the 5-CB, 8-CB and ZLI-1185 experiments in Figure 2.6, it was shown that the ZLI-1185 (1.13 μm) selected for an intermediate length between 5-CB (1.83 μm) and 8-CB (0.81 μm).

Table 2.1: Compilation of experimental data between different liquid crystals used

	8-CB	5-CB	ZLI-1185
Density (CNT/μm^2)	0.81	0.39	0.53
Std. Dev. in Alignment ($^{\circ}$)	29	33	45
Length (μm)	0.81	1.83	1.13

Given how close the distribution in length is in the ZLI-1185 trials as with previous 5-CB and 8-CB reports, it can be assumed that liquid crystal selection plays an impact on the length selectivity. Density and lengths aside, alignment is where ZLI-1185 trials took the

most notable hit as illustrated in Figure 2.5. The standard deviation in the alignment using ZLI-1185 (45 °) was the largest in comparison to 5-CB (33 °) and 8-CB (29 °) trials. Further, the histogram belonging to ZLI-1185 lost its Gaussian distribution. It has been documented that 8-CB produces enhanced alignment in comparison to 5-CB as a result of the more ordered smectic A phase being used[126] and it seems ZLI-1185 made that juxtaposition even more drastic. ZLI-1185 proved to be a disappointment in providing supportive data for the case of using elevated temperatures for enhancing the ART.

Seeing that the nematic nature of ZLI-1185 might have interfered with the results obtained at an elevated temperature a second attempt was performed with a different liquid crystal. Pentyl 4'-(decyloxy)-[1,1'-biphenyl]-4-carboxylate **(11)**, unlike ZLI-1185, exhibits a smectic A mesophase between 53 °C and 82 °C.[127]

Unfortunately, multiple trials using this liquid crystal did not provide any nanotube deposition on the surface of the silicon substrates after synthesis as shown in Figure A.24. Despite the use of a more ordered liquid crystal, the intrinsic ability for this liquid crystal to align **(5)** might not be as great as the previous liquid crystals employed. Further, it was realized that the time at which functionalization occurs could also be quite important. If the molecules functionalize onto the surface prior to precipitation of the ordered smectic A phase, then there would be a lack of anisotropic ordering. From previous experiments, a silicon control in which no alignment method was used during the functionalization yielded no nanotube deposition.[99] This could perhaps be an analogous situation, especially since the kinetics of the functionalization is not known. With multiple unknown parameters presented simultaneously, the endeavor to explore functionalizations at higher temperatures was abandoned.

2.4 Iptycene Alteration

Selectivity is important to enhance homogeneity within the electronic properties of manufactured devices. One of the tenants that the ART suggests is that CNT diameter selectivity can be controlled by modifying the size of the iptycene pockets.[99] We explore the validity of this proposal by designing a second generation iptycene molecule with a smaller pocket.

A liquid crystal mixture was made with 8-CB and iptycene **(9)**. Iterations of the ART were subsequently performed. Disappointingly, no CNT's were present on the surface after AFM analysis. Images of these trials were identical to the ones shown in Figure A.24. Puzzled by this outcome, literature was consulted to see if there were any clues as to why this came

about. An indication appeared while searching through Swager's work as he had suggested that alignment of the iptycene in liquid crystal media is directly proportional to the size of the pockets.[99] Since the size of (9) was effectively shrunk by more than 50% laterally in comparison to (5), effective alignment of these molecules in the liquid crystal medium is a valid concern. As a result, efforts to continue with this molecule were abandoned.

2.5 Magnetic Field Alignment

Up until now, alignment layers were used align the liquid crystal mixtures. Despite achieving success, these alignment layers possess intrinsic degrees of alignment, are non-reusable and expose the active area of the substrates to dust through physical contact.[128,129] Switching to a non-contact form of alignment such as magnetic or electric fields would negate all of the aforementioned crutches and thus, advance the ART through improved performance and device fabrication compatibility while reducing cost in the long run. Figure 2.7 shows a schematic of the altered ART process.
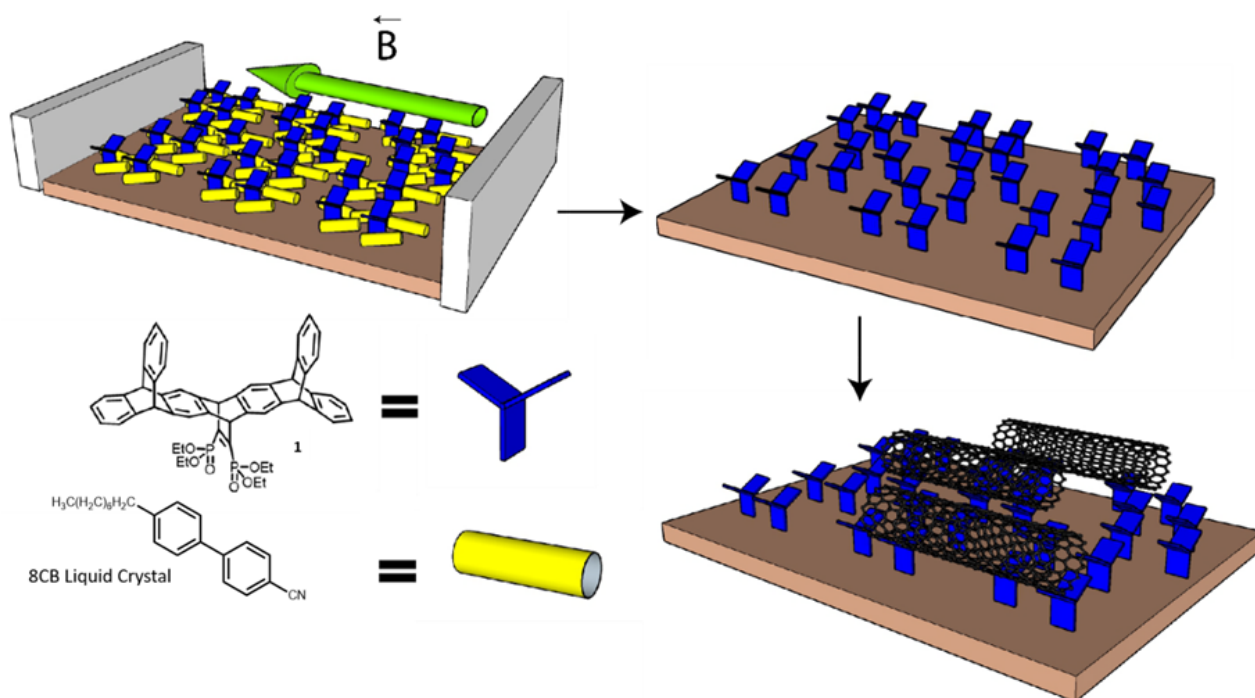

Figure 2.7: Schematic of the ART with magnetic fields

27
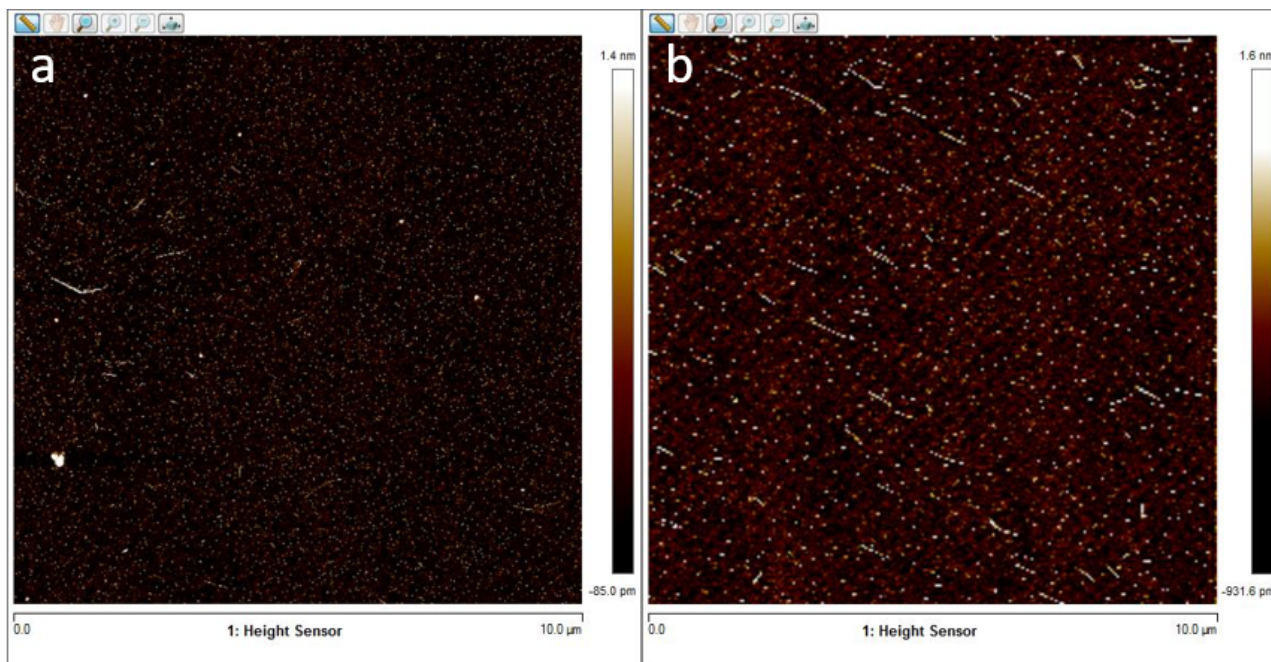
Figure 2.8: a) AFM image of a silicon shard using 0.6 T alignment apparatus after the modified ART. The full set of images can be found in Figure A.6 b) AFM image of a silicon shard using 0.9 T alignment apparatus after the modified ART. The full set of images can be found in Figure A.7. White dots are artifacts that appear sometimes while using the AFM

Prior to performing any functionalization, the (1.3 mol%) 8-CB/iptycene (5) mixture was first analyzed on an in-house polarized optical microscope[130] setup to confirm homogeneity in the smectic A phase of the 8-CB mixture in a magnetic field (Figure A.22). Spots of imperfection were found in the 0.6 T image while complete homogeneity was found in the 0.9 T trial. Once a working knowledge of the surface was identified, he modified ART process began by depositing a thin layer of liquid crystal/iptycene mixture onto a silicon shard which was subsequently placed inside a 0.6 T magnetic alignment apparatus. After a two day functionalization at room temperature, the shard was then rinsed with solvent and placed in a CNT solution for deposition. Initial results obtained were below expectations as tube density was low at 0.11 CNT/μm^2 as shown in Figure Figure 2.8a. The performance of the alignment was also poor with tubes scattered in all directions with no organized distribution (Figure 2.9). Optimism for the altered ART process increased when the magnetic field strength was increased to 0.9 T (Figure Figure 2.8b) as tube density
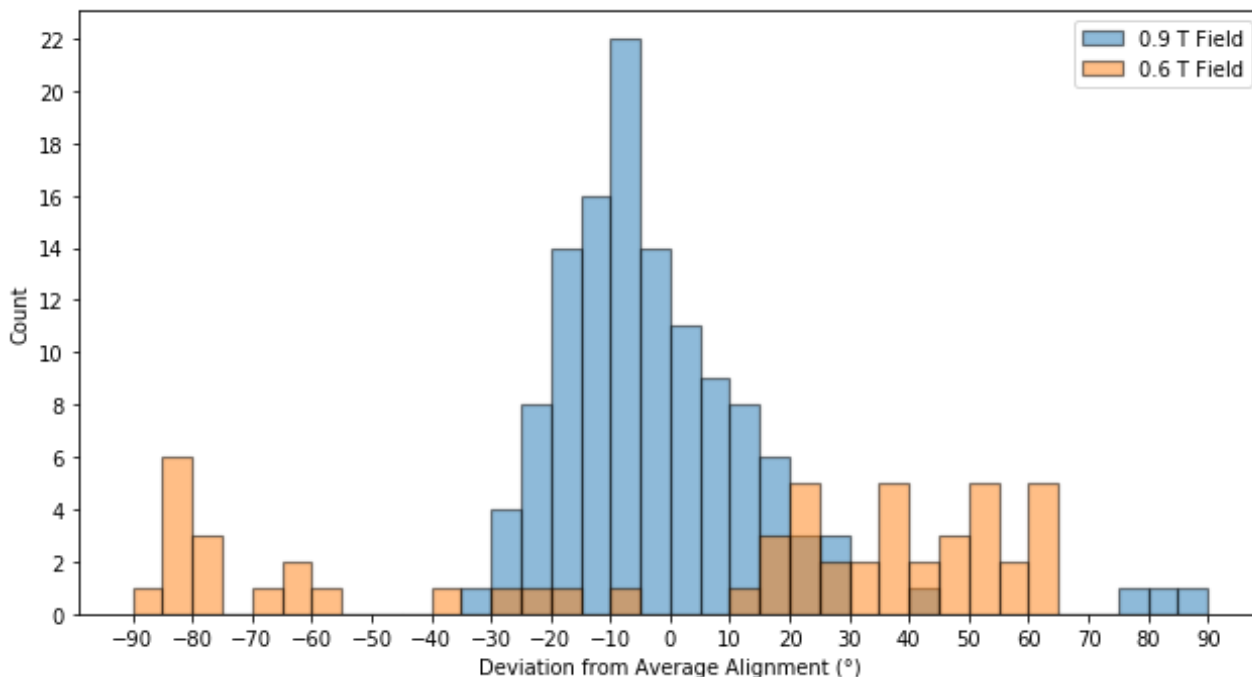
Figure 2.9: Combined alignment histogram of 0.6 T and 0.9 T experiments

tripled to 0.3 CNT/μm² with a clear Gaussian distribution in Figure 2.9. Quantitatively, 90% of CNT's can be found in within one standard deviation of the mean.

Imperfections in homogeneity in the 0.6 T environment proved to be a decisive factor in dictating CNT density and alignment. Functionalization kinetics could have also played a role since the time required to establish the uniform smectic A phase is also important. As there is a parallel process of iptycene functionalization occurring while the mixture is aligning, molecular order can be compromised depending on when this occurs. Thus, it is imperative for the smectic phase to precipitate as quickly as possible to achieve maximum order. Since molecular alignment occurs much quicker in a higher field environment,[141] the molecules are much more likely to be attached in an ordered fashion and relay the alignment information to the CNT's. A positive correlation can be established between alignment and density with magnetic field strength.

Performance from magnetic field alignment were slightly lower in comparison to the results obtained from the alignment layer. This conclusion is solely based off of the density ob-

Table 2.2: Combined Alignment Trials with 8-CB

Method	Alignment		Length		
	Centre of Distribution (°)	Std. Deviation (°)	Mean (µm)	Std. Deviation (µm)	Density (CNT/µm²)
0.6 T	0	55	0.57	0.22	0.11
0.9 T	0.53	24	0.38	0.14	0.3
Alignment Layer	0	29	0.68	N/A	0.81

tained as the value from the 0.9 T magnetic field (0.3 CNT/µm²) was still less than half of that from the alignment layer (0.81 CNT/µm²). Given that density saw an improvement after increasing the magnetic field from 0.6 T to 0.9 T, an even greater enhancement might be seen if an even higher magnetic field strength is used.
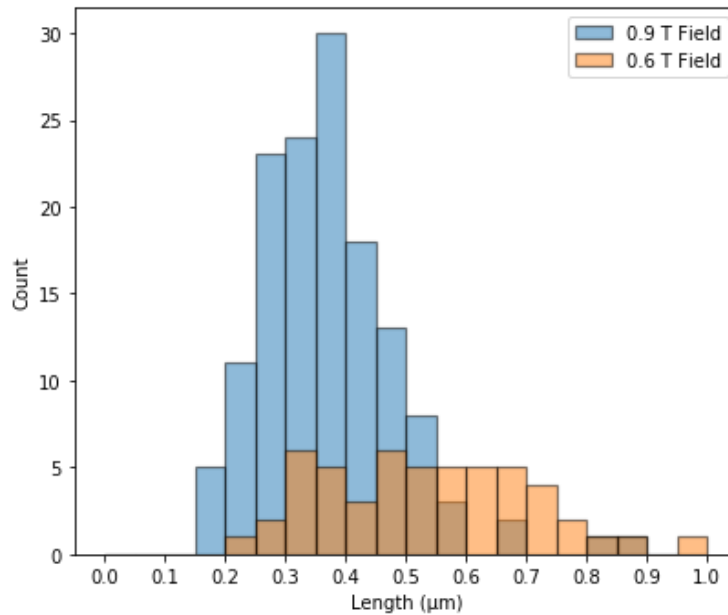

Figure 2.10: Combined length histogram of 0.6 T and 0.9 T experiments

A trend can also be identified in Figure 2.10 between magnetic field strength and the length of the selected CNT's. The average length of the CNT's for the 0.6 T trial was 0.57 µm +/- 0.22 µm, whereas the 0.9 T trial measured 0.38 µm +/- 0.14 µm, which suggests that

field strength has an inverse relationship to CNT length. This can possibly be attributed to stronger magnetic fields creating shorter segments of aligned molecules to preserve the thermodynamic state of the aligned liquid crystal. What is interesting to note is that this average length (0.38 μm) is almost half the size of the average length obtained from using the alignment layer (0.68 μm). In the original report, 8-CB was observed to select for shorter CNT's in comparison to 5-CB (0.68 μm vs 1.53 μm).[126] The use of magnetic fields seemed to have enhanced the intrinsic length selectivity of the 8-CB liquid crystal even further. As a comparison, standard deviation in the alignment was 5 º lower between the 0.9 T magnetic field and alignment layer but that is easily within a margin of error. Thus, magnetic fields plays a significant role in selecting for lengths of the CNT's.

A dropcast of the commercial CNT mixture probed under a 633 nm laser in Figure Figure 2.11b reveals the (17,4) fold to be the predominant chirality while the (15,8) and (12,5) folds are the next two in abundance. After subjection to the modified ART condition under a 0.6 T magnetic field, the (17,4) and (12,5) folds decreased dramatically in relative intensity, leaving the (15,8) fold to be the predominant type of CNT deposited. In addition to the aforementioned folds, it was revealed that peaks corresponding to (16,6), (14,7), (15,3), (16,1) and (9,9) were found on the surface as removal of other folds improved the definition of the peaks in the spectrum. Magnetic alignment under a 0.6 T magnetic field proved to be effective in sorting out the CNT's. Upon subjection to a 0.9 T magnetic field however, the performance had unexpectedly decreased. Referring to Figure Figure 2.11b once again, the peaks had decayed in definition. This is indicative of decreased selectivity as the presence of other nanotube folds can broaden individual signals much akin to the original dropcast sample. Nevertheless, the (17,4) and (12,5) folds to be the major discernible peaks remaining. An anomalous trait that is shared between the sets of Raman data is that the peaks are offset by varying degrees between the different samples. This error seems systematic as each peak within the same sample is offset by a standard value. Literature suggests that environmental factors play a significant role in the discrepancies in the radial breathing mode (RBM) scattering frequencies between different samples.[132,133] Results from this modified ART are consistent with selectivity results from previous reports as the (15,8) and (17,4) folds correspond to 1.59 nm and 1.44 nm respectively in diameter.[93,134]

The spectrum in Figure Figure 2.11c obtained with the 532 nm laser reveals a sorting relationship more in line with our expectations with an increasing magnetic field. A broad shoulder was revealed between 160 – 185 cm^{-1} upon subjection of the unprocessed drop-cast sample to the laser, indicating a rich mixture of chiralities. After an iteration of the magnetic alignment under a 0.6 T field, peaks, though still broad, corresponding to (17,6),
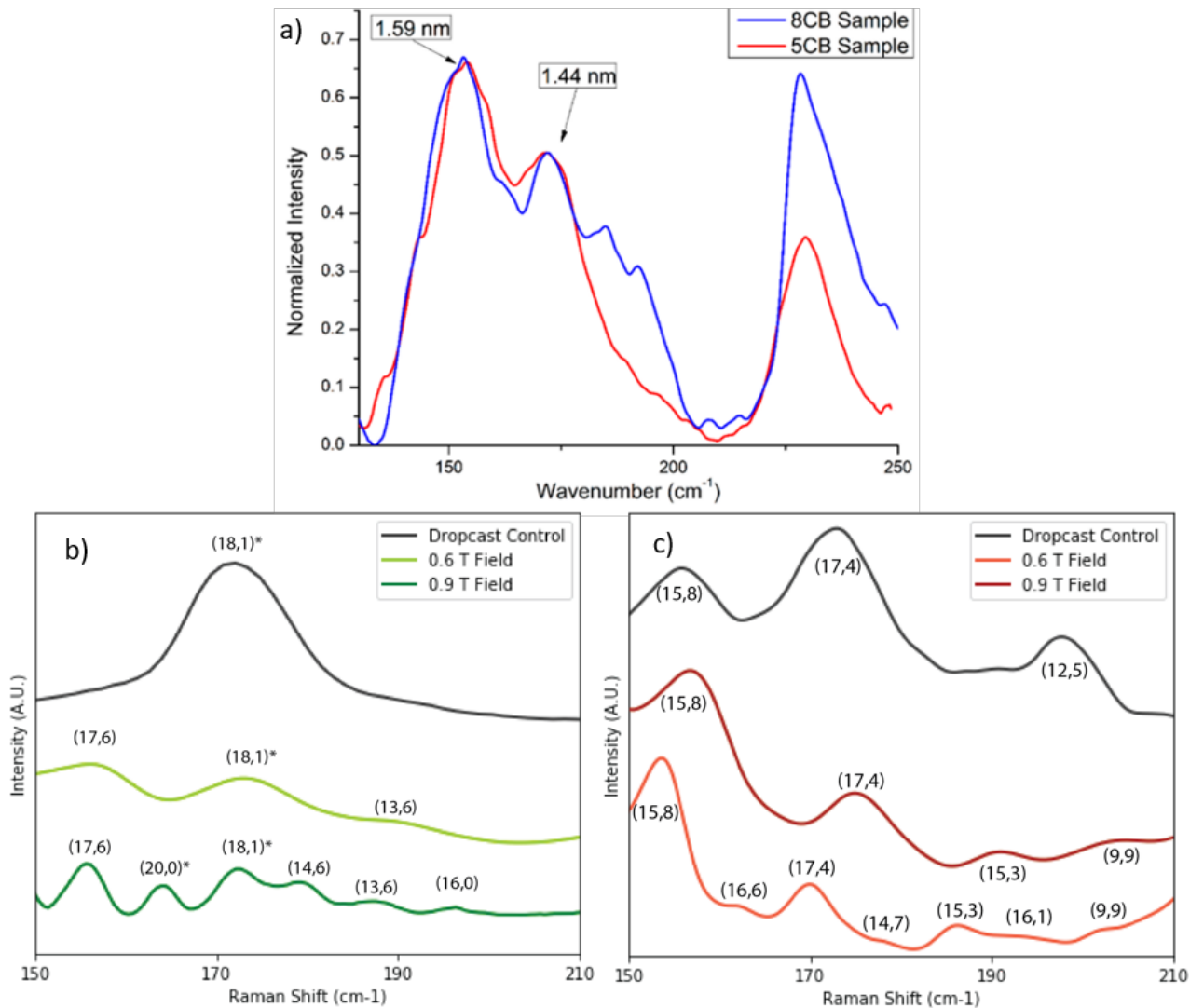
Figure 2.11: a) 633 nm Raman spectra of original ART trials with 8-CB and 5-CB[126] b) Combined Raman spectra using 633 nm incident laser. Sloping towards the end of the spectrum is caused by the onset Raman peak of iptycene **1** c) Combined Raman spectra using 532 nm incident laser. Asterisks (*) indicate the fold matching closest to the peak as there are others very close in proximity. Alternatively, the (20,0) could be a (19,2), while the (18,1) could also be (17,3) or (13,8)

(18,1) and (13,6) were exposed indicating that some folds were eliminated by the built-in sorting function of the ART. A subsequent increase in magnetic field strength to 0.9 T suggests enhancement of sorting action with the 532 nm laser. This is demonstrated by the decrease in intensity from the (17,6) fold as well as other chiralities leading to further increased definition of the RBM peaks. As a result, folds that were revealed include: (20,0), (14,6) and (16,0). The demonstration of sorting is achieved using magnetic alignment albeit, the relationship between strength of magnetic field and its effect on sorting remains inconclusive. This may have to do with the relative positioning of the iptycene on the surface as slight misalignment may create a different preference for certain folds.

Chapter 3

Conclusion

In conclusion, we successfully prepared the preliminary tools needed to enhance the ART. We first built a POM in order to observe the dynamics in our liquid crystal mixture. In this section, we constructed an economical POM with a heating stage and digital connection for facile recording of data, totaling about $150-$200. Demonstrations were performed on liquid crystals under magnetic fields and at different temperatures to verify its versatility. We then made target molecules used to probe various aspects of the ART. Initial difficulty was encountered in trying to improve the synthetic route for the original iptycene (**5**). Despite seeing success in the inital two Diels Alder steps, the last dehydration was unsuccessful as a result of an inability to recreate literature conditions. This setback was overshadowed however with the successful synthesis of subsequent liquid crystal and iptycene molecules. Liquid crystal (**11**) was made through two nucleophilic additions using 4-Hydroxy-4-biphenylcarboxylic acid, while the second generation iptycene (**9**) was made through a direct attachment of the phosphonate ester anchoring group to an intermediate that occurred during the synthesis of the original iptycene. These preparations allowed us to proceed with ART experimentation.

We used the molecules we made to change various elements of the ART, allowing us to gain mechanistic insights during the process. Specifically, we altered the liquid crystal/temperature and iptycene size parameters of the process. Initial trials of using ZLI-1185 at 70 ºC did not yield better performance in comparison to results obtained at room temperature with both 8-CB and 5-CB. Standard deviations in the alignment were the highest in ZLI-1185 while density only improved a modest amount in comparison to 5-CB but lagged behind the results from 8-CB. CNT lengths obtained through ZLI-1185 were in between 8-CB and 5-CB indicating that liquid crystal selection does indeed play a role in length selectivity. The nematic nature of ZLI-1185 was hypothesized to interfere with

the results obtained at a higher temperature. However, this hypothesis was not able to be verified as conducting the elevated temperature experiment with a smectic A liquid crystal **(11)** did not yield any CNT deposition. It was at this point that we realized that elevated temperatures might actually be working against us since iptycene functionalization and liquid crystal alignment were occurring simultaneously. Thus, if the former occurs before the latter, no order would be established and thus no CNT deposition would occur. Another attempt was made to better understand the mechanism by altering the iptycene design. The size of the iptycene pockets was shrunk in iptycene **(9)** to see if it had an impact on CNT diameter selection. This effort came with an unexpected result in which again, no CNT deposition was observed. Consulting with literature, this observation seemed consistent with a decreasing ability to align iptycene molecules in liquid crystal media as the size of the iptycene pockets shrunk. Thus, attempts to improve the performance of the ART failed but valuable insight was obtained regarding the mechanistic underpinnings.

In addition to the mechanistic insights, low strength magnetic fields were used to successfully align and sort CNT's. We have qualitatively outlined positive relationships between magnetic field strength and properties such as density, alignment and length selectivity. Diameter selectivity based on field strength is inconclusive as data from the 532 nm and 633 nm lasers show conflicting information: the 532 nm showed best selectivity was achieved under a 0.9 T field while 633 nm suggested that the 0.6 T was the most optimal condition. Regardless, despite needing further data to establish a pattern between field strength and diameter selectivity, general selectivity patterns remain congruent with previous reports. Despite having lower performance in comparison to the alignment layer, magnetic field integration can be thought of as an evolution of the ART. This is due to the potential in further enhancing the results through increased magnetic fields and noticeable advantages such as reusability of the alignment apparatus improving economic viability. Further, as this technique does not rely on physical contact of the active area with potentially dusty surfaces, nano-electronic processing compatibility is preserved. Adequate development of this process can potentially yield a low cost solution to a challenging task facing the future of nano-electronic processing.

Chapter 4

References

(1) Freud, S. Mourning and Melancholia. In *The Standard Edition of the Complete Psychological Works of Sigmund Freud, Volume XIV (1914-1916): On the History of the Psycho-Analytic Movement, Papers on Metapsychology and Other Works*; The Hogarth Press: London, 1917; pp 237–258.

(2) Frankl, V. E.; Kushner, H.; Winslade, W. *Man's Search for Meaning*; Beacon Press: Boston, 2006.

(3) Marshall, M. *Logotherapy Revisited: Review of the Tenets of Viktor E. Frankl's Logotherapy*; Ottawa Institute of Logotherapy: Ottawa, 2012.

(4) Nouri, A. A brief history of lobotomy https://www.aaas.org/brief-history-lobotomy.

(5) Salzer, H. M. Anxiety and Depressive States Treated With Isonicotinyl Hydrazide (Isoniazid). *Arch. Neurol. Psychiatry* **1953**, *70* (3), 317.

(6) Lemere, F. Isoniazid Treatment of Psychiatric Patients. *Arch. Neurol. Psychiatry* **1954**, *71* (5), 624.

(7) Vaishnavi, S. N.; Nemeroff, C. B.; Plott, S. J.; Rao, S. G.; Kranzler, J.; Owens, M. J. Milnacipran: A Comparative Analysis of Human Monoamine Uptake and Transporter

Binding Affinity.*Biol. Psychiatry* **2004**, *3223* (03), 320.

(8) Owens, M. J.; Morgan, W. N.; Plott, S. J.; Nemeroff, C. B. Neurotransmitter Receptor and Transporter Binding Profile of Antidepressants and Their Metabolites. *J. Pharmacol. Exp. Ther.* **1997**, 283 (3), 1305.

(9) Davis, J. M. Efficacy of Tranquilizing and Antidepressant Drugs. *Arch. Gen. Psychiatry* **1965**, *13* (6), 552.

(10) Cole, J. O. Therapeutic Efficacy of Antidepressant Drugs: A Review. *J. Am. Med. Assoc.* **1964**, *190* (5), 448.

(11) Brigitta, B. Pathophysiology of Depression and Mechanisms of Treatment. *Dialogues Clin. Neurosci.* **2002**, *4* (1), 7.

(12) Marek, G. J.; Carpenter, L. L.; McDougle, C. J.; Price, L. H. Synergistic Action of 5-HT2a Antagonists and Selective Serotonin Reuptake Inhibitors in Neuropsychiatric Disorders. *Neuropsychopharmacology* **2003**, *28* (2), 402.

(13) Bergström, J.; Hultman, E. A Study of the Glycogen Metabolism during Exercise in Man. *Scand. J. Clin. Lab. Invest.* **1967**, *19* (3), 218.

(14) Cosgrove, D. J. Relaxation in a High-Stress Environment: The Molecular Bases of Extensible Cell Walls and Cell Enlargement. *Plant Cell Online* **2002**, *9* (7), 1031.

(15) History National Museum of American. *American Chemical Society National Historic Chemical Landmarks. Bakelite: The World's First Synthetic Plastic*; 1993.

(16) Kohan, M. I. The History and Development of Nylon 6,6. In *High Performance Polymers: Their Origins and Development*; Elsevier: New York, 1986.

(17) Plastics Insight. Polyester Production, Price and Market Forecast https://www.plasticsinsight.com/r intelligence/resin-prices/polyester/.

(18) Gabara, V. High-Performance Fibers. *Ullmann's Encyclopedia of Industrial Chemistry*; Wiley, 2016.

(19) Seechurn, C. C. C. J.; Kitching, M. O.; Colacot, T. J.; Snieckus, V. Palladium-Catalyzed Cross-Coupling: A Historical Contextual Perspective to the 2010 Nobel Prize. *Angew. Chemie - Int. Ed.* **2012**, *51* (21), 5062.

(20) The Royal Swedish Academy of Sciences. *Palladium-Catalyzed Cross Couplings in Organic Synthesis*; 2010.

(21) Nakabayashi, K. Direct Arylation Polycondensation as Conjugated Polymer Synthesis Methodology. *Polym. J.* **2018**, *50*, 475.

(22) Tsuchiya, K.; Ogino, K. Catalytic Oxidative Polymerization of Thiophene Derivatives. *Polym. J.* **2013**, *45* (3), 281.

(23) Niemi, V. M.; Knuuttila, P.; Österholm, J. E.; Korvola, J. Polymerization of 3-Alkylthiophenes with FeCl3. *Polymer* **1992**, *33* (7), 1559.

(24) McCullough, R. D.; Lowe, R. D.; Jayaraman, M.; Anderson, D. L. Design, Synthesis, and Control of Conducting Polymer Architectures: Structurally Homogeneous Poly(3-Alkylthiophenes). *J. Org. Chem.* **1993**, *58* (4), 904.

(25) Hayashi, S.; Kojima, Y.; Koizumi, T. Highly Regioselective Pd/C-Catalyzed Direct Arylation toward Thiophene-Based π-Conjugated Polymers. *Polym. Chem.* **2015**, *6* (6), 881.

(26) Gobalasingham, N. S.; Noh, S.; Thompson, B. C. Palladium-Catalyzed Oxidative Direct Arylation Polymerization (Oxi-DArP) of an Ester-Functionalized Thiophene. *Polym. Chem.* **2016**, *7* (8), 1623.

(27) StatNano. *A Statistical Report on Nanotechnology Research Publications*; 2017.

(28) Bae, S.; Kim, H.; Lee, Y.; Xu, X.; Park, J. S.; Zheng, Y.; Balakrishnan, J.; Lei, T.; Ri Kim, H.; Song, Y. Il; Kim, Y. J.; Kim, K. S.; Özyilmaz, B.; Ahn, J. H.; Hong, B. H.;

Iijima, S. Roll-to-Roll Production of 30-Inch Graphene Films for Transparent Electrodes. *Nat. Nanotechnol.* **2010**, *5* (8), 574.

(29) Lipomi, D. J.; Tee, B. C. K.; Vosgueritchian, M.; Bao, Z. Stretchable Organic Solar Cells. *Adv. Mater.* **2011**, *23* (15), 1771.

(30) Gelinck, G. H.; Huitema, H. E. A.; Veenendaal, E. Van; Cantatore, E.; Schrijnemakers, L.; Van Der Putten, J. B. P. H.; Geuns, T. C. T.; Beenhakkers, M.; Giesbers, J. B.; Huisman, B. H.; Meijer, E. J.; Benito, E. M.; Touwslager, F. J.; Marsman, A. W.; Van Rens, B. J. E.; De Leeuw, D. M. Flexible Active-Matrix Displays and Shift Registers Based on Solution-Processed Organic Transistors. *Nat. Mater.* **2004**, *3* (2), 106.

(31) Kim, D.; Viventi, J.; Amsden, J.; Xiao, J.; Vigeland, L.; Kim, Y.; Blanco, J.; Litt, B.; Rogers, J. Dissolvable Films of Silk Fibroin for Ultrathin Conformal Bio-Integrated Electronics. *Nat. Mater.* **2010**, *9*, 511.

(32) Wu, S.-T.; Luo, Z. OLED Versus LCD: Who Wins? http://lcd.creol.ucf.edu/Publications/2015/19-21-OptInnov-Feb15.pdf.

(33) Fukuda, Y.; Watanabe, T.; Wakimoto, T.; Miyaguchi, S.; Tsuchida, M. Organic LED Display Exhibiting Pure RGB Colors. *Synth. Met.* **2000**, 111, 1.

(34) Das, R.; Ghaffarzadeh, K.; He, X. *OLED Display Forecasts and Technologies 2019-2029: The Global Rise of Flexible and Foldable Displays*; 2018.

(35) U.S. Energy Information Administration. International Energy Outlook 2017. *Int. Energy Outlook* **2017**, IEO2017, 143.

(36) Papalexiou, S. M.; Aghakouchak, A. Global, Regional, and Megacity Trends in the Highest Temperature of the Year: Diagnostics and Evidence for Accelerating Trends Earth's Future. *Earth's Futur.* **2014**, *6*, 71.

(37) Cox, P. M.; Huntingford, C.; Williamson, M. S. Emergent Constraint on Equilibrium Climate Sensitivity from Global Temperature Variability. *Nature* **2018**, *553* (7688), 319.

(38) Manser, J. S.; Christians, J. A.; Kamat, P. V. Intriguing Optoelectronic Properties of Metal Halide Perovskites. *Chem. Rev.* **2016**, *116* (21), 12956.

(39) Rong, Y.; Hu, Y.; Mei, A.; Tan, H.; Saidaminov, M. I.; Seok, S. Il; McGehee, M. D.; Sargent, E. H.; Han, H. Challenges for Commercializing Perovskite Solar Cells. *Science* **2018**, 361.

(40) Xie, S.; Li, W.; Pan, Z.; Chang, B.; Lianfeng, S. Mechanical and Physical Properties on Carbon Nanotube. *J. Phys. Chem. Solids* **2000**, *61* (7), 1153–1158.

(41) Duong, H. M.; Einarsson, E.; Okawa, J.; Xiang, R.; Maruyama, S. Thermal Degradation of Single-Walled Carbon Nanotubes. *Jpn. J. Appl. Phys.* **2008**, 47, 1994.

(42) Bati, A. S. R.; Yu, L.; Batmunkh, M.; Shapter, J. G. Synthesis, Purification, Properties and Characterization of Sorted Single-Walled Carbon Nanotubes. *Nanoscale* **2018**, *10* (47), 22087–22139.

(43) Deria, P.; Sinks, L. E.; Park, T. H.; Tomezsko, D. M.; Brukman, M. J.; Bonnell, D. A.; Therien, M. J. Phase Transfer Catalysts Drive Diverse Organic Solvent Solubility of Single-Walled Carbon Nanotubes Helically Wrapped by Ionic, Semiconducting Polymers. *Nano Lett.* **2010**, *10* (10), 4192–4199.

(44) Adenuga, A. A.; Truong, L.; Tanguay, R. L.; Remcho, V. T. Preparation of Water Soluble Carbon Nanotubes and Assessment of Their Biological Activity in Embryonic Zebrafish. *Int. J. Biomed. Nanosci. Nanotechnol.* **2013**, *3* (1/2), 38.

(45) Peng, H.; Alemany, L. B.; Margrave, J. L.; Khabashesku, V. N. Sidewall Carboxylic Acid Functionalization of Single-Walled Carbon Nanotubes. *J. Am. Chem. Soc.* **2003**, *125* (49), 15174–15182.

(46) Setaro, A.; Adeli, M.; Glaeske, M.; Przyrembel, D.; Bisswanger, T.; Gordeev, G.; Maschietto, F.; Faghani, A.; Paulus, B.; Weinelt, M.; Arenal, R.; Haag, R.; Reich, S. Preserving π-Conjugation in Covalently Functionalized Carbon Nanotubes for Optoelectronic Applications. *Nat. Commun.* **2017**, *8*, 1-7.

(47) Zhang, H.; Wu, B.; Hu, W.; Liu, Y. Separation and/or Selective Enrichment of Single-Walled Carbon Nanotubes Based on Their Electronic Properties. *Chem. Soc. Rev.* **2011**, *40* (3), 1324.

(48) Joselevich, E.; Dai, H.; Liu, J.; Hata, K.; Windle, A. H. Carbon Nanotube Synthesis and Organization. *Top. Appl. Phys.* **2008**, *164* (2008), 101.

(49) Zhang, D.; Yang, J.; Yang, F.; Li, R.; Li, M.; Ji, D.; Li, Y. (N,m) Assignments and Quantification for Single-Walled Carbon Nanotubes on SiO2/Si Substrates by Resonant Raman Spectroscopy. *Nanoscale* **2015**, 7, 10719.

(50) Peng, L. M.; Zhang, Z.; Wang, S. Carbon Nanotube Electronics: Recent Advances. *Mater. Today* **2014**, *17* (9), 433.

(51) Zhang, F.; Hou, P.-X.; Liu, C.; Cheng, H.-M. Epitaxial Growth of Single-Wall Carbon Nanotubes. *Carbon* **2016**, 102, 181–197.

(52) Rao, R.; Pint, C. L.; Islam, A. E.; Weatherup, R. S.; Hofmann, S.; Meshot, E. R.; Wu, F.; Zhou, C.; Dee, N.; Amama, P. B.; Carpena-Nuñez, J.; Shi, W.; Plata, D. L.; Penev, E. S.; Yakobson, B. I.; Balbuena, P. B.; Bichara, C.; Futaba, D. N.; Noda, S.; Shin, H.; Kim, K. S.; Simard, B.; Mirri, F.; Pasquali, M.; Fornasiero, F.; Kauppinen, E. I.; Arnold, M.; Cola, B. A.; Nikolaev, P.; Arepalli, S.; Cheng, H.-M.; Zakharov, D. N.; Stach, E. A.; Zhang, J.; Wei, F.; Terrones, M.; Geohegan, D. B.; Maruyama, B.; Maruyama, S.; Li, Y.; Adams, W. W.; Hart, A. J. Carbon Nanotubes and Related Nanomaterials: Critical Advances and Challenges for Synthesis toward Mainstream Commercial Applications. *ACS Nano* **2018**, *12* (12), 11756.

(53) Bachilo, S. M.; Strano, M. S.; Kittrell, C.; Hauge, R. H.; Smalley, R. E.; Weisman, R. B. Structure-Assigned Optical Spectra of Single-Walled Carbon Nanotubes. *Science* **2002**, *298* (5602), 2361.

(54) Hu, Y.; Kang, L.; Zhao, Q.; Zhong, H.; Zhang, S.; Yang, L.; Wang, Z.; Lin, J.; Li, Q.; Zhang, Z.; Peng, L.; Liu, Z.; Zhang, J. Growth of High-Density Horizontally Aligned SWNT Arrays Using Trojan Catalysts. *Nat. Commun.* **2015**, *6*, 6099.

(55) White, C. T.; Todorov, T. N. Carbon Nanotubes as Long Ballistic Conductors. *Nature* **1998**, *393*, 240.

(56) Franklin, A. D. Carbon Nanotube Electronics. In *Emerging Nanoelectronic Devices*; 2015; pp 315–335.

(57) Dong, G.; Zhao, J.; Shen, L.; Xia, J.; Meng, H.; Yu, W.; Huang, Q.; Han, H.; Liang, X.; Peng, L. Large-Area and Highly Uniform Carbon Nanotube Film for High-Performance Thin Film Transistors. *Nano Res.* **2018**, *11* (8), 4356.

(58) Kauffman, D. R.; Star, A. Electronically Monitoring Biological Interactions with Carbon Nanotube Field-Effect Transistors. *Chem. Soc. Rev.* **2008**, *37* (6), 1197.

(59) Han, B.; Xue, X.; Xu, Y.; Zhao, Z.; Guo, E.; Liu, C.; Luo, L.; Hou, H. Preparation of Carbon Nanotube Film with High Alignment and Elevated Density. *Carbon* **2017**, 122, 496.

(60) Esawi, A. M. K.; Farag, M. M. Carbon Nanotube Reinforced Composites: Potential and Current Challenges. *Mater. Des.* **2007**, *28* (9), 2394.

(61) Yao, S.; Zhu, Y. Nanomaterial-Enabled Stretchable Conductors: Strategies, Materials and Devices. *Adv. Mater.* **2015**, *27* (9), 1480.

(62) Xu, F.; Sun, L. X.; Zhang, J.; Qi, Y. N.; Yang, L. N.; Ru, H. Y.; Wang, C. Y.; Meng, X.; Lan, X. F.; Jiao, Q. Z.; Huang, F. L. Thermal Stability of Carbon Nanotubes. *J. Therm. Anal. Calorim.* **2010**, *102* (2), 785.

(63) Yao, Z.; Kane, C. L.; Dekker, C. High-Field Electrical Transport in Single-Wall Carbon Nanotubes. *Phys. Rev. Lett.* **2000**, *84* (13), 2941–2944.

(64) Park, S.; Vosguerichian, M.; Bao, Z. A Review of Fabrication and Applications of Carbon Nanotube Film-Based Flexible Electronics. *Nanoscale* **2013**, *5* (5), 1727.

(65) Purewal, M. S.; Hong, B. H.; Ravi, A.; Chandra, B.; Hone, J.; Kim, P. Scaling of Resistance and Electron Mean Free Path of Single-Walled Carbon Nanotubes. *Phys. Rev.*

Lett. **2007**, *98* (18), 2.

(66) Qiu, C.; Zhang, Z.; Peng, L. M. Scaling Carbon Nanotube CMOS FETs towards Quantum Limit. In *International Electron Devices Meeting, IEDM*; IEEE, 2017; Vol. Part F1343, 5.5.1.

(67) Qiu, C.; Zhang, Z.; Zhong, D.; Si, J.; Yang, Y.; Peng, L. M. Carbon Nanotube Feedback-Gate Field-Effect Transistor: Suppressing Current Leakage and Increasing on/off Ratio. *ACS Nano* **2015**, *9* (1), 969.

(68) Jun Kang, S.; Kocabas, C.; Ozel, T. High-Performance Electronics Using Dense, Perfectly Aligned Arrays of Single-Walled Carbon Nanotubes. *Nat. Nanotechnol.* **2007**, *2*, 230–236.

(69) Kim, S.; Kim, S.; Park, J.; Ju, S.; Mohammadi, S. Fully Transparent Pixel Circuits Driven by Random Network Carbon Nanotube Transistor Circuitry. *ACS Nano* **2009**, *4* (6).

(70) Sarker, B. K.; Shekhar, S.; Khondaker, S. I. Semiconducting Enriched Carbon Nanotube Aligned Arrays of Tunable Density and Their Electrical Transport Properties. *ACS Nano* **2011**, *5* (8), 6297.

(71) Moaiyeri, M. H.; Rahi, A.; Sharifi, F.; Navi, K. Design and Evaluation of Energy-Efficient Carbon Nanotube FET-Based Quaternary Minimum and Maximum Circuits. *J. Appl. Res. Technol.* **2017**, *15* (3), 233.

(72) Wang, F.; Kozawa, D.; Miyauchi, Y.; Hiraoka, K.; Mouri, S.; Ohno, Y.; Matsuda, K. Considerably Improved Photovoltaic Performance of Carbon Nanotube-Based Solar Cells Using Metal Oxide Layers. *Nat. Commun.* **2015**, *6*, 1–7.

(73) Shastry, T. A.; Hersam, M. C. Carbon Nanotubes in Thin-Film Solar Cells. *Adv. Energy Mater.* **2017**, *7* (10), 1–15.

(74) Li, X.; Jung, Y.; Sakimoto, K.; Goh, T. H.; Reed, M. A.; Taylor, A. D. Improved Efficiency of Smooth and Aligned Single Walled Carbon Nanotube/Silicon Hybrid Solar

Cells. *Energy Environ. Sci.* **2013**, *6* (3), 879–887.

(75) Allen, B. L.; Kichambare, P. D.; Star, A. Carbon Nanotube Field-Effect-Transistor-Based Biosensors. *Adv. Mater.* **2007**, *19* (11), 1439.

(76) Li, J.; Lu, Y.; Ye, Q.; Cinke, M.; Han, J.; Meyyappan, M. Carbon Nanotube Sensors for Gas and Organic Vapor Detection. *Nano Lett.* **2003**, *3* (7), 929.

(77) Qi, P.; Vermesh, O.; Grecu, M.; Javey, A.; Wang, Q.; Dai, H.; Peng, S.; Cho, K. J. Toward Large Arrays of Multiplex Functionalized Carbon Nanotube Sensors for Highly Sensitive and Selective Molecular Detection. *Nano Lett.* **2003**, *3* (3), 347.

(78) Gao, C.; Guo, Z.; Liu, J. H.; Huang, X. J. The New Age of Carbon Nanotubes: An Updated Review of Functionalized Carbon Nanotubes in Electrochemical Sensors. *Nanoscale* **2012**, *4* (6), 1948.

(79) Roberts, M.; Lemieux, M. C.; Bao, Z. Sorted and Aligned Single-Walled Carbon Nanotube Networks for Transistor-Based Aqueous Chemical Sensors. *ACS Nano* **2009**, *3* (10), 3287.

(80) He, M.; Jiang, H.; Liu, B.; Fedotov, P. V.; Chernov, A. I.; Obraztsova, E. D.; Cavalca, F.; Wagner, J. B.; Hansen, T. W.; Anoshkin, I. V.; Obraztsova, E. A.; Belkin, A. V.; Sairanen, E.; Nasibulin, A. G.; Lehtonen, J.; Kauppinen, E. I. Chiral-Selective Growth of Single-Walled Carbon Nanotubes on Lattice-Mismatched Epitaxial Cobalt Nanoparticles. *Sci. Rep.* **2013**, 3, 1.

(81) Wang, J.; Jin, X.; Liu, Z.; Yu, G.; Ji, Q.; Wei, H.; Zhang, J.; Zhang, K.; Li, D.; Yuan, Z.; Li, J.; Liu, P.; Wu, Y.; Wei, Y.; Wang, J.; Li, Q.; Zhang, L.; Kong, J.; Fan, S.; Jiang, K. Growing Highly Pure Semiconducting Carbon Nanotubes by Electrotwisting the Helicity. *Nat. Catal.* **2018**, 1, 326.

(82) Xu, B.; Kaneko, T.; Shibuta, Y.; Kato, T. Preferential Synthesis of (6 , 4) Single-Walled Carbon Nanotubes by Controlling Oxidation Degree of Co Catalyst. *Sci. Rep.* **2017**, No. August, 1.

(83) Gupta, M. P.; Behnam, A.; Lian, F.; Estrada, D.; Pop, E.; Kumar, S. High Field Breakdown Characteristics of Carbon Nanotube Thin Film Transistors. *Nanotechnology* **2013**, *24* (40).

(84) Buh, G. H.; Hwang, J. H.; Jeon, E. K.; So, H. M.; Lee, J. O.; Kong, K. J.; Chang, H. On-Chip Electrical Breakdown of Metallic Nanotubes for Mass Fabrication of Carbon-Nanotube-Based Electronic Devices. *IEEE Trans. Nanotechnol.* **2008**, *7* (5), 624–627.

(85) Li, J.; Franklin, A. D.; Liu, J. Gate-Free Electrical Breakdown of Metallic Pathways in Single-Walled Carbon Nanotube Crossbar Networks. *Nano Lett.* **2015**, *15* (9), 6058.

(86) Arnold, M. S.; Green, A. A.; Hulvat, J. F.; Stupp, S. I.; Hersam, M. C. Sorting Carbon Nanotubes by Electronic Structure Using Density Differentiation. *Nat. Nanotechnol.* **2006**, *1* (1), 60.

(87) Reis, W. G.; Weitz, R. T.; Kettner, M.; Kraus, A.; Schwab, M. G.; Tomović, Ž.; Krupke, R.; Mikhael, J. Highly Efficient and Scalable Separation of Semiconducting Carbon Nanotubes via Weak Field Centrifugation. *Sci. Rep.* **2016**, No. March, 1–11.

(88) Tahara, K.; Ishikawa, T.; Hirsch, B. E.; Kubo, Y.; Brown, A.; Eyley, S.; Daukiya, L.; Thielemans, W.; Li, Z.; Walke, P.; Hirose, S.; Hashimoto, S.; De Feyter, S.; Tobe, Y. Self-Assembled Monolayers as Templates for Linearly Nanopatterned Covalent Chemical Functionalization of Graphite and Graphene Surfaces. *ACS Nano* **2018**, *12*, acsnano.8b06681.

(89) Cao, Q.; Rogers, J. A. Random Networks and Aligned Arrays of Single-Walled Carbon Nanotubes for Electronic Device Applications. *Nano Res.* **2008**, *1* (4), 259.

(90) Tune, D. D.; Stolz, B. W.; Pfohl, M.; Flavel, B. S. Dry Shear Aligning: A Simple and Versatile Method to Smooth and Align the Surfaces of Carbon Nanotube Thin Film. *Nanoscale* **2016**, *8*, 3232.

(91) He, X.; Gao, W.; Xie, L.; Li, B.; Zhang, Q.; Lei, S.; Robinson, J. M.; Hroz, E. H.; Doorn, S. K.; Wang, W.; Vajtai, R.; Ajayan, P. M.; Adams, W. W.; Hauge, R. H.; Kono, J. Wafer-Scale Monodomain Films of Spontaneously Aligned Single-Walled Carbon Nan-

otubes. *Nat. Nanotechnol.* **2016**, *11* (7), 633.

(92) Ma, Y.; Wang, B.; Wu, Y.; Huang, Y.; Chen, Y. The Production of Horizontally Aligned Single-Walled Carbon Nanotubes. *Carbon* **2011**, 49, 4098.

(93) Gao, W.; Doiron, C. F.; Li, X.; Kono, J.; Naik, G. V; Doiron, C. F.; Li, X.; Kono, J.; Naik, G. V. Macroscopically Aligned Carbon Nanotubes as a Refractory Platform for Hyperbolic Thermal Emitters. *ACS Photonics* **2019**, *6*, 1602.

(94) Reina, A.; Hofmann, M.; Zhu, D.; Kong, J. Growth Mechanism of Long and Horizontally Aligned Carbon Nanotubes by Chemical Vapor Deposition. *J. Phys. Chem. C* **2007**, *111*(20), 7292–7297.

(95) Iakoubovskii, K. Techniques of Aligning Carbon Nanotubes. *Cent. Eur. J. Phys.* **2009**, *7* (4), 645.

(96) Cole, M. T.; Milne, W. I. Plasma Enhanced Chemical Vapour Deposition of Horizontally Aligned Carbon Nanotubes. *Materials* **2013**, *6* (6), 2262.

(97) Ural, A.; Li, Y.; Dai, H. Electric-Field-Aligned Growth of Single-Walled Carbon Nanotubes on Surfaces. *Appl. Phys. Lett.* **2002**, 81, 3464.

(98) Huang, S.; Cai, X.; Liu, J.; V, D. U.; Carolina, N. Growth of Millimeter-Long and Horizontally Aligned Single-Walled Carbon Nanotubes on Flat Substrates. *J. Am. Chem. Soc.* **2003**, *125* (19), 5636–5637.

(99) Selmani, S.; Schipper, D. J. Orientation Control of Molecularly Functionalized Surfaces Applied to the Simultaneous Alignment and Sorting of Carbon Nanotubes. *Angew. Chemie - Int. Ed.* **2018**, *57* (9), 2399.

(100) Stöhr, J.; Samant, M. G. Liquid Crystal Alignment by Rubbed Polymer Surfaces: A Microscopic Bond Orientation Model. *J. Electron Spectros. Relat. Phenomena* **1999**, *98-99* (January), 189.

(101) Rego, J. A.; Harvey, J. A. A.; MacKinnon, A. L.; Gatdula, E. Asymmetric Synthesis of a Highly Soluble "trimeric" Analogue of the Chiral Nematic Liquid Crystal Twist Agent Merck S1011. *Liq. Cryst.* **2010**, *37* (1), 37.

(102) Ishihara, S.; Wakemoto, H.; Nakazima, K.; Matsuo, Y. The Effect of Rubbed Polymer Films on the Liquid Crystal Alignment. *Liq. Cryst.* **1989**, *4* (6), 669.

(103) Koshida, N.; Kikui, S. Magnetic Field Assisted Alignment of Nematic Liquid Crystal on a Polymeric Surface. *Appl. Phys. Lett.* **1982**, *40* (6), 541.

(104) De Oliveira, B. F.; Avelino, P. P.; Moraes, F.; Oliveira, J. C. R. E. Nematic Liquid Crystal Dynamics under Applied Electric Fields. *Phys. Rev.* **2010**, *82* (4), 1.

(105) Griffiths, D. J. Introduction to Electrodynamics, 4th ed.; Cambridge University Press, 2017.

(106) Dunmur, D. A.; Miller, W. H. Dipole-Dipole Correlation in Nematic Liquid Crystals. *Mol. Cryst. Liq. Cryst.* **1980**, *60* (4), 281–292.

(107) Kosa, T.; Palffy-muhoray, P. Magnetic Field Induced Deformations in Nematic Liquid Crystals. *Liq. Cryst. Today* **1996**, *6* (1), 7–8.

(108) Buka, A.; de Jeu, W. H. Diamagnetism and Orientational Order of Nematic Liquid Crystals. *J. Phys. Paris* **1982**, *43* (6), 361–367.

(109) Hart, H. Iptycenes, Cuppedophanes and Cappedophanes. *Pure Appl. Chem.* **1993**, *65* (1), 27.

(110) Long, T. M.; Swager, T. M. Minimization of Free Volume: Alignment of Triptycenes in Liquid Crystals and Stretched Polymers. *Adv. Mater.* **2001**, *13* (8), 601.

(111) Tournus, F.; Latil, S.; Heggie, M. I.; Charlier, J. Pi -Stacking Interaction between Carbon Nanotubes and Organic Molecules. *Phys. Rev. B* **2005**, *72* (075431), 1.

(112) Selmani, S. Exploiting the Potential of Carbon Nanotubes and Fullerenes Through Their Interaction with Specially Designed π-Conjugated Iptycenes, 2020.

(113) Bürgi, T. Properties of the Gold-Sulphur Interface: From Self-Assembled Monolayers to Clusters. *Nanoscale* **2015**, *7* (38), 15553–15567.

(114) Pujari, S. P.; Scheres, L.; Marcelis, A. T. M.; Zuilhof, H. Covalent Surface Modification of Oxide Surfaces. *Angew. Chemie - Int. Ed.* **2014**, *53* (25), 6322–6356.

(115) Chen, X.; Luais, E.; Darwish, N.; Ciampi, S.; Thordarson, P.; Gooding, J. J. Studies on the Effect of Solvents on Self-Assembled Monolayers Formed from Organophosphonic Acids on Indium Tin Oxide. *Langmuir* **2012**, *28* (25), 9487–9495.

(116) Cattani-Scholz, A.; Pedone, D.; Dubey, M.; Neppl, S.; Nickel, B.; Feulner, P.; Schwartz, J.; Absteiter, G.; Tornow, M. Organophosphonate-Based PNA-Functionalization of Silicon Nanowires for Label-Free DNA Detection. *ACS Nano* **2008**, *2* (8), 1653–1660.

(117) Ma, H.; Acton, O.; Hutchins, D. O.; Cernetic, N.; Jen, A. K. Y. Multifunctional Phosphonic Acid Self-Assembled Monolayers on Metal Oxides as Dielectrics, Interface Modification Layers and Semiconductors for Low-Voltage High-Performance Organic Field-Effect Transistors. *Phys. Chem. Chem. Phys.* **2012**, *14* (41),14110–14126.

(118) T. S.; Thissen, P.; Peixoto, T.; Longo, R. C.; Peng, W.; Schmidt, W. G.; Cho, K.; Chabal, Y. J. Activation of Surface Hydroxyl Groups by Modification of H-Terminated Si(111) Surfaces. *J. Am. Chem. Soc.* **2012**, *134* (21), 8869.

(119) Oweimreen, G. A. On the Nature of the Smectic A-to-Nematic Phase Transition of 8CB. *J. Phys. Chem. B* **2001**, *105* (35), 8417–8419.

(120) Chandrasekhar, S.; Krishnamurti, D. Birefringence of Nematic Liquid Crystals.*Liq. Cryst. Today* **1966**, *23* (7), 459.

(121) Zou, Y.; Namkung, J.; Lin, Y.; Ke, D.; Lindquist, R. Interference Colors of Nematic Liquid Crystal Films at Different Applied Voltages and Surface Anchoring Conditions.*Opt. Express* **2011**, *19* (44), 3297.

(122) Hart, H.; Raju, N.; Meador, M. A.; Ward, D. L. Synthesis of Heptiptycenes with Face-to-Face Arene Rings via a 2,3:6,7-Anthradiyne Equivalent. *J. Org. Chem.* **1983**, *48* (23), 4357.

(123) Pestov, S. Subvolume A · 1.05: 47 - 2664. In *Landolt-Börnstein - Group VIII Advanced Materials and Technologies*; Springer Materials, 2003.

(124) Pestov, S. Subvolume A · 2.1.1:226 - 581. In *Landolt-Börnstein - Group VIII Advanced Materials and Technologies*; Springer Materials, 2003.

(125) Denolf, K.; Cordoyiannis, G.; Glorieux, C.; Thoen, J. Effect of Nonmesogenic Impurities on the Liquid Crystalline Phase Transitions of Octylcyanobiphenyl. Phys. Rev. E - Stat. Nonlinear, *Soft Matter Phys.* **2007**, *76* (5), 1.

(126) Selmani, S.; Hawes, G. F.; Schipper, D. J. Liquid-Crystal Phase Optimization Using the Alignment Relay Technique for the Deposition of Single-Walled Carbon Nanotubes. *ACS Appl. Nano. Mater.* **2020**, *3* (3), 2118.

(127) LCI Systems. LiqCryst. 2019.

(128) Patel, J. S.; Leslie, T. M.; Goodby, J. W. A Reliable Method of Alignment for Smectic Liquid Crystals. *Ferroelectrics* **1984**, *59* (1), 137.

(129) Hassanein, G. N.; Chan, H. P.; Uddin, A. Improvement in Rise Time of Liquid Crystals with Patterned Benzocyclobutene as Alignment Layer for Photonic Applications. *Optoelectron. Adv. Mater. Commnications* **2009**, *3* (10), 1083.

(130) Wang, S.; Schipper, D. J. Constructing a Low-Cost Polarized Optical Microscope for Undergraduate Material-Characterization Studies. *J. Chem. Educ.* **2019**, *96* (4), 823–826.

(131) Moore, J. S.; Stupp, S. I. Orientation Dynamics of Main-Chain Liquid Crystal Polymers. 2. Structure and Kinetics in a Magnetic Field. *Macromolecules* **1987**, 20, 282.

(132) Lefebvre, J.; Fraser, J. M.; Homma, Y.; Finnie, P. Photoluminescence from Single-Walled Carbon Nanotubes: A Comparison between Suspended and Micelle-Encapsulated

Nanotubes. *App. Phys. A* **2004**, 78, 1107.

(133) Araujo, P. T.; Maciel, I. O.; Pesce, P. B. C.; Pimenta, M. A.; Doorn, S. K.; Qian, H.; Hartschuh, A.; Steiner, M.; Grigorian, L.; Hata, K. Nature of the Constant Factor in the Relation between Radial Breathing Mode Frequency and Tube Diameter for Single-Wall Carbon Nanotubes. *Phys. Rev. B* **2008**, *77* (241403), 1.

(134) Snowdon, M. R.; Selmani, S.; Schipper, D. J. Sonication-Enhanced Alignment Relay Technique for the Orientation of Single-Walled Carbon Nanotubes. *ACS Appl. Nano Mater.* **2019**, 2, 6637.

(135) Nagamine, T.; Januszko, A.; Ohta, K.; Kaszynski, P.; Endo, Y. The Effect of the Linking Group on Mesogenic Properties of Three-Ring Derivatives of p-Carborane and Biphenyl. *Liq. Cryst.* **2008**, *35* (7), 865.

(136) Maruyama, S. Kataura Plot for Resonant Raman
http://www.photon.t.u-tokyo.ac.jp/ maruyama/kataura/kataura.html.

APPENDICES

Appendix A

Supplementary Information

Solvents used in synthesis were high performance liquid chromatography grade. Toluene that was used was taken from a solvent purification system. Solvents used for column chromatography were reagent grade and used as purchased. All solvents and reagents used were purchased from Sigma-Aldrich Co. with the exception of bis(diethoxyphosphoryl) acetylene, which was purchased from STREM Chemicals, Inc. 90% surfactant coated, 90% semiconducting polymer wrapped single-walled carbon nanotubes were purchased from NanoIntegris Inc while the rubbed polyimide alignment layers were purchased from Instec, Inc.

^{1}H-NMR experiments were performed at room temperature on a Bruker AVANCE300 (300 MHz) with an internal standard reference to CDCl3. ^{13}C-NMR spectra were obtained on a Bruker AVANCE300 (75.5 MHz) NMR spectrometer with the same internal standard. ^{31}P-NMR was taking on a Bruker AVANCE300 (121.5 MHz) with 85% phosphoric acid in water as the internal standard. The following abbreviations were used for the NMR peak multiplicities: s, singlet ; t, triplet ; dd, doublet of doublets ; m, multiplet . Chemical shifts were reported in parts per million (ppm) relative to $CDCl_3$; δ= 7.26 ppm as the calibration peaks for ^{1}H-NMR and δ= 77.0 ppm for ^{13}C-NMR. [31]P signal was measured in reference to 0 ppm for phosphoric acid for compound (**5**).

# A.1   Synthetic Procedure and NMR Spectra
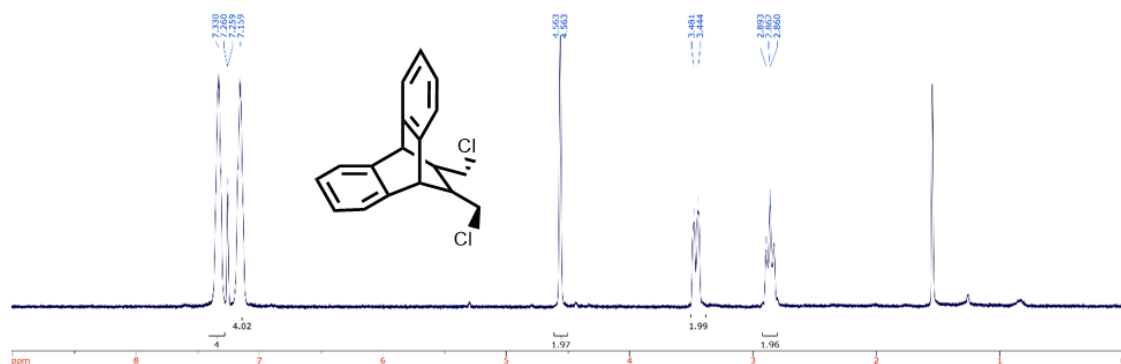
Figure A.1: ^{1}H NMR Spectra of **(1)**

Procedure was followed according to literature.[99] An off-white powder was obtained in a 65% yield.

^{1}H-NMR (300 MHz, CDCl$_3$) δ: 7.33 ppm (m, 4H), 7.17 ppm (m, 4H), 4.44 ppm (s, 2H), 3.32 ppm (dd, 2H, 5.1 Hz, 9.8 Hz), 2.99 ppm (dd, 2H, 9.2 Hz, 10.9 Hz)
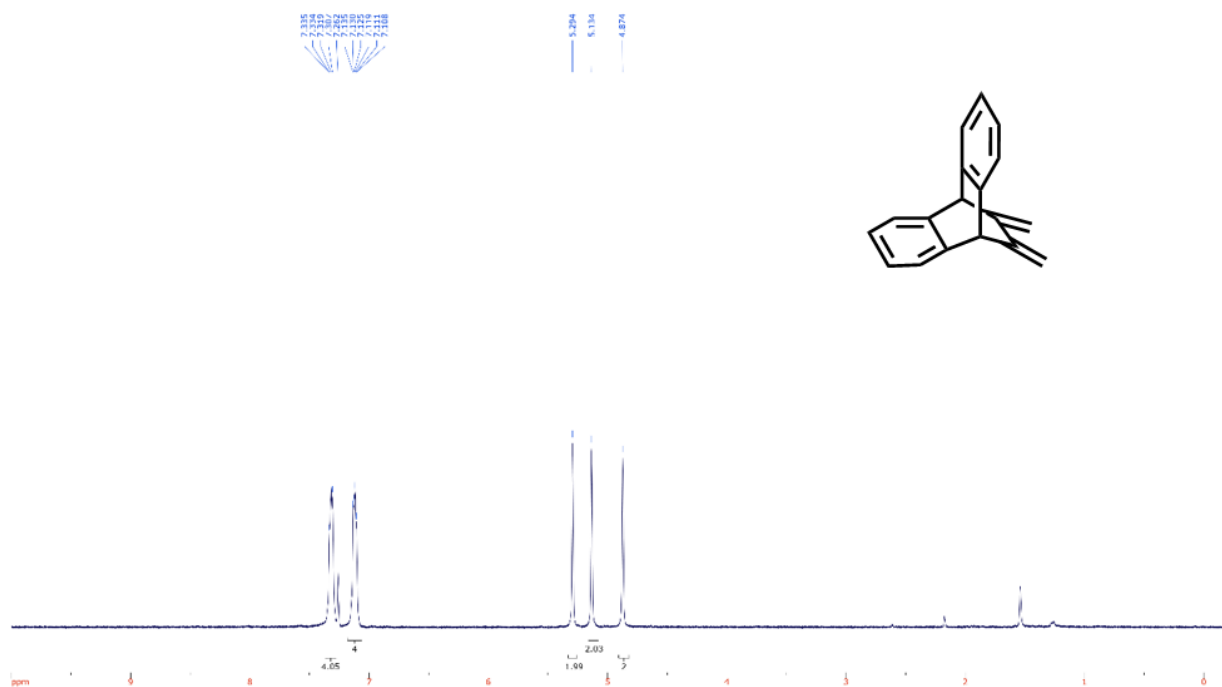
Figure A.2: ^{1}H NMR Spectra of **(2)**

Procedure was followed according to literature.[99] A yellowish-white solid was obtained in a 80% yield.

^{1}H-NMR (300 MHz, CDCl$_3$) δ: 7.32 ppm (m, 4H), 7.11 ppm (m, 4H), 5.29 ppm (s, 2H), 5.13 ppm (s, 2H), 4.87 ppm (s, 2H)
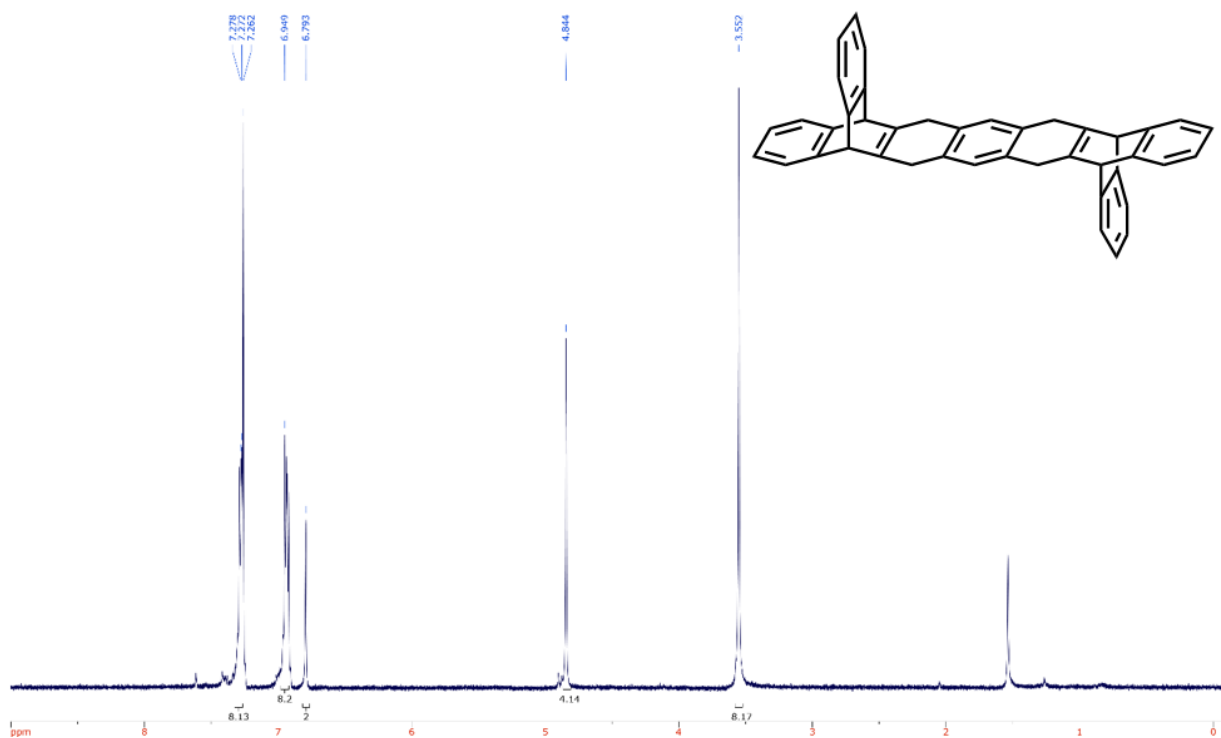
Figure A.3: ^{1}H NMR Spectra of **(3)**

Procedure was followed according to literature.[99] A white solid was produced in a 58% yield.

^{1}H-NMR (300 MHz, CDCl$_3$) δ: 7.28 ppm (m, 8H), 6.95 ppm (m, 8H), 4.84 ppm (s, 4H), 3.55 ppm (s, 8H)
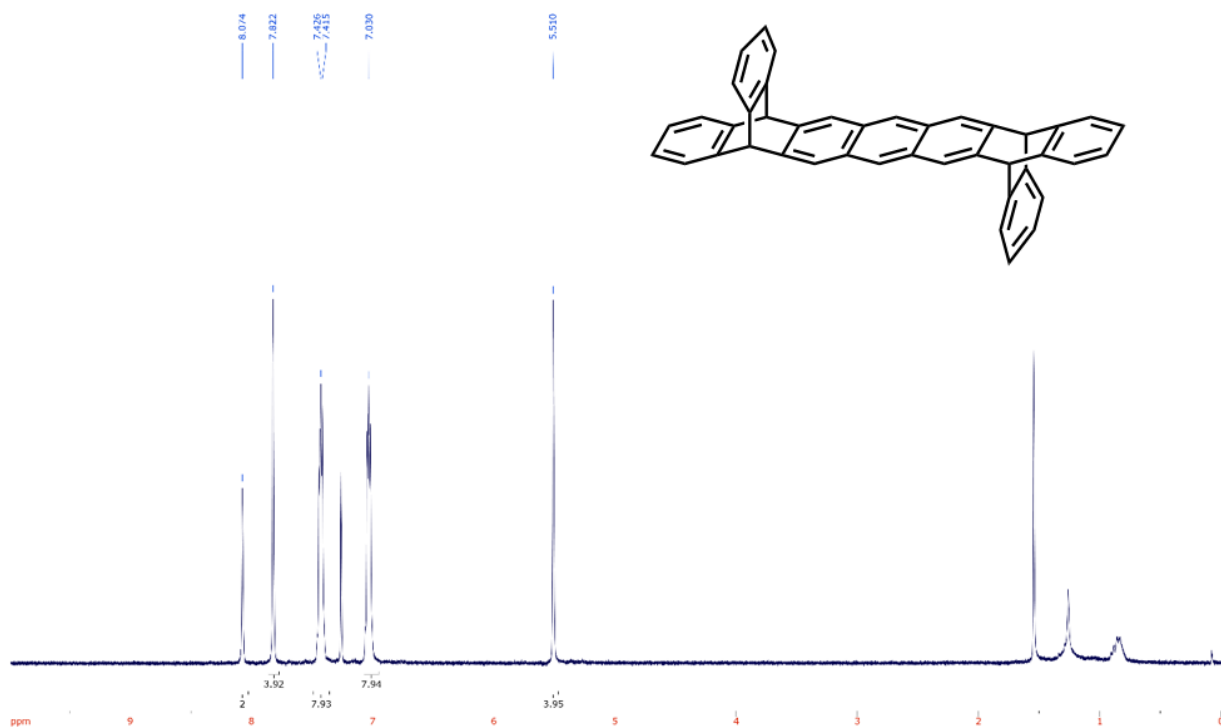
Figure A.4: ^{1}H NMR Spectra of **(4)**

Both procedures were followed according to literature.[99,120] A white solid was obtained in a 70% yield for the Pd/C route, while a 2% yield was obtained for the elimination route.

^{1}H-NMR (300 MHz, CDCl$_3$) δ: 8.07 ppm (s, 2H), 7.82 ppm (s, 4H), 7.43 ppm (m, 8H), 7.03 ppm (m, 8H), 5.51 ppm (s, 4H)
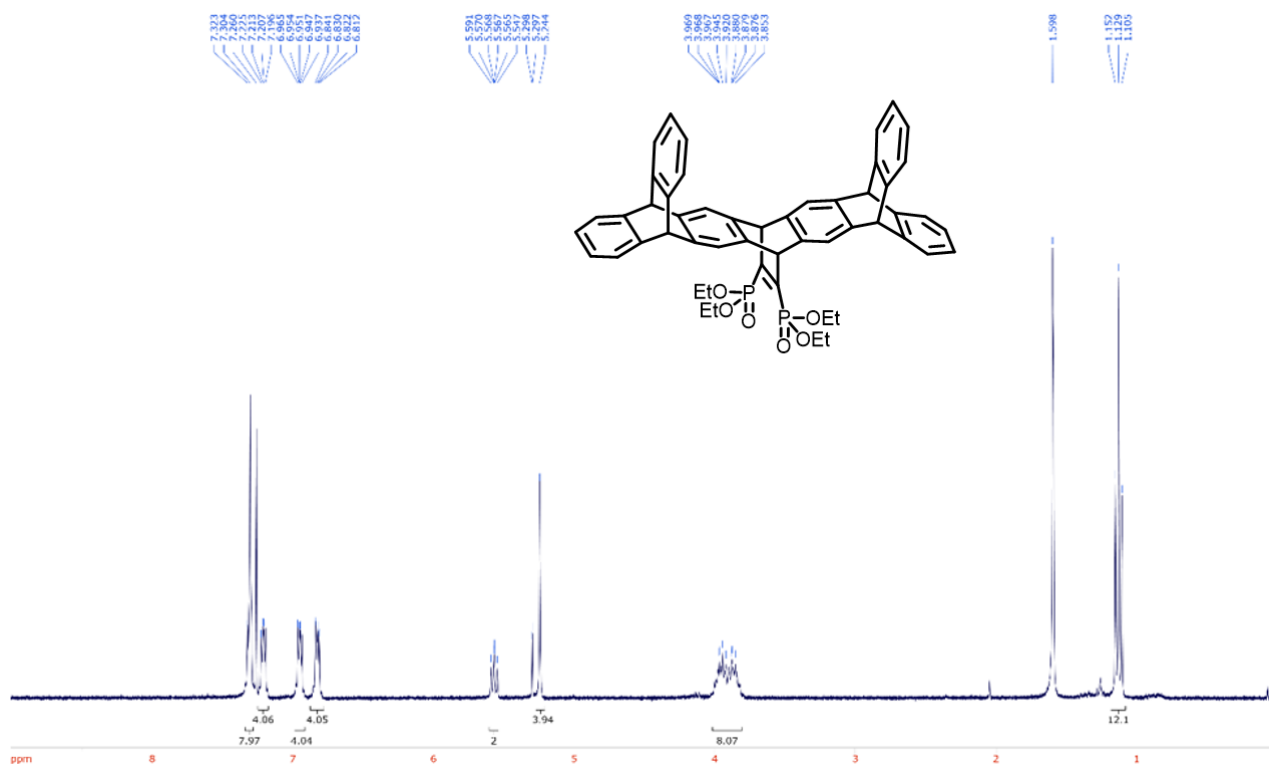
Figure A.5: ^{1}H NMR Spectra of **(5)**

Procedure was followed according to literature.[99] A white solid was obtained in a 30% yield.

^{1}H-NMR (300 MHz, CDCl$_3$) δ: 7.30 ppm (m, 8H), 7.21 ppm (m, 4H), 6.96 ppm (m, 4H), 6.82 (m, 4H), 5.57 ppm (t, 2H, 6.7 Hz), 5.24 ppm (s, 4H), 3.94 ppm (m, 8H). 1.13 ppm (t, 12H, 7.2 Hz).
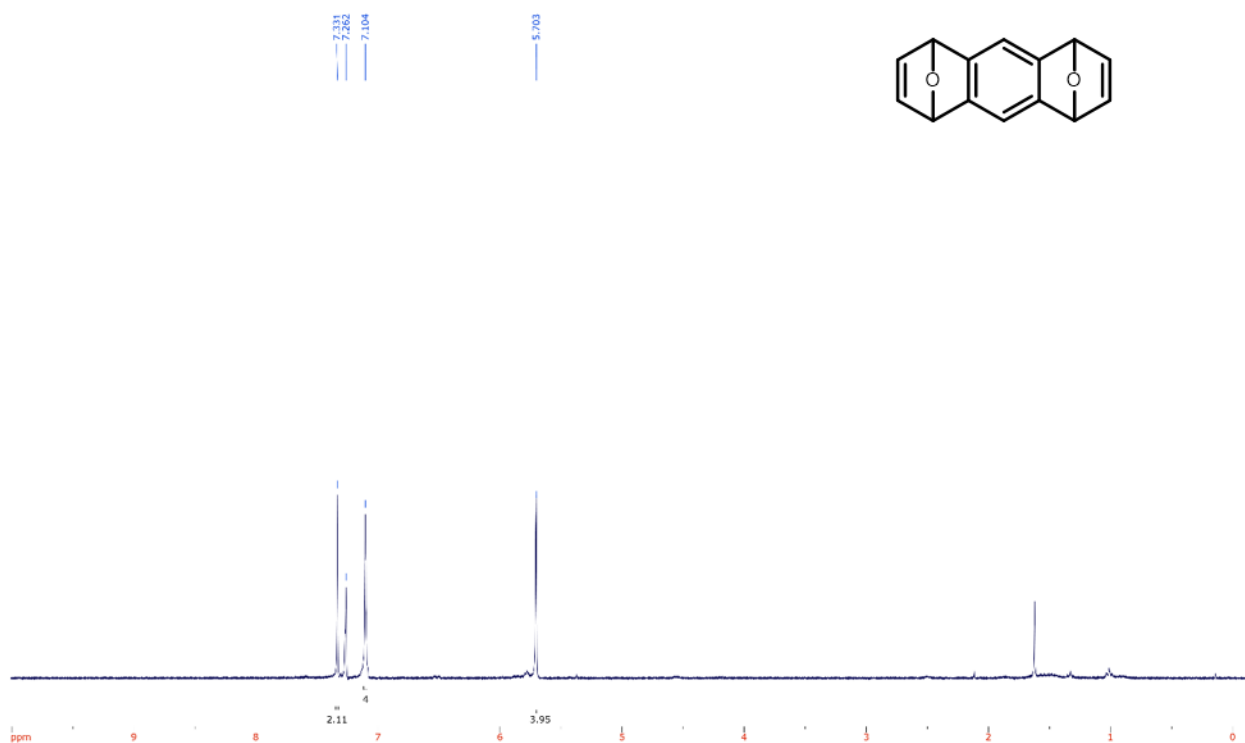
Figure A.6: ^{1}H NMR Spectra of **(6)**

Procedure was followed according to literature.[137] Both diasteromers resembled an off-white solid and were obtained in a combined 54% yield.

^{1}H-NMR (300 MHz, CDCl$_3$) δ: 7.33 ppm (s, 2H), 7.10 ppm (s, 4H), 5.70 ppm (s, 4H)
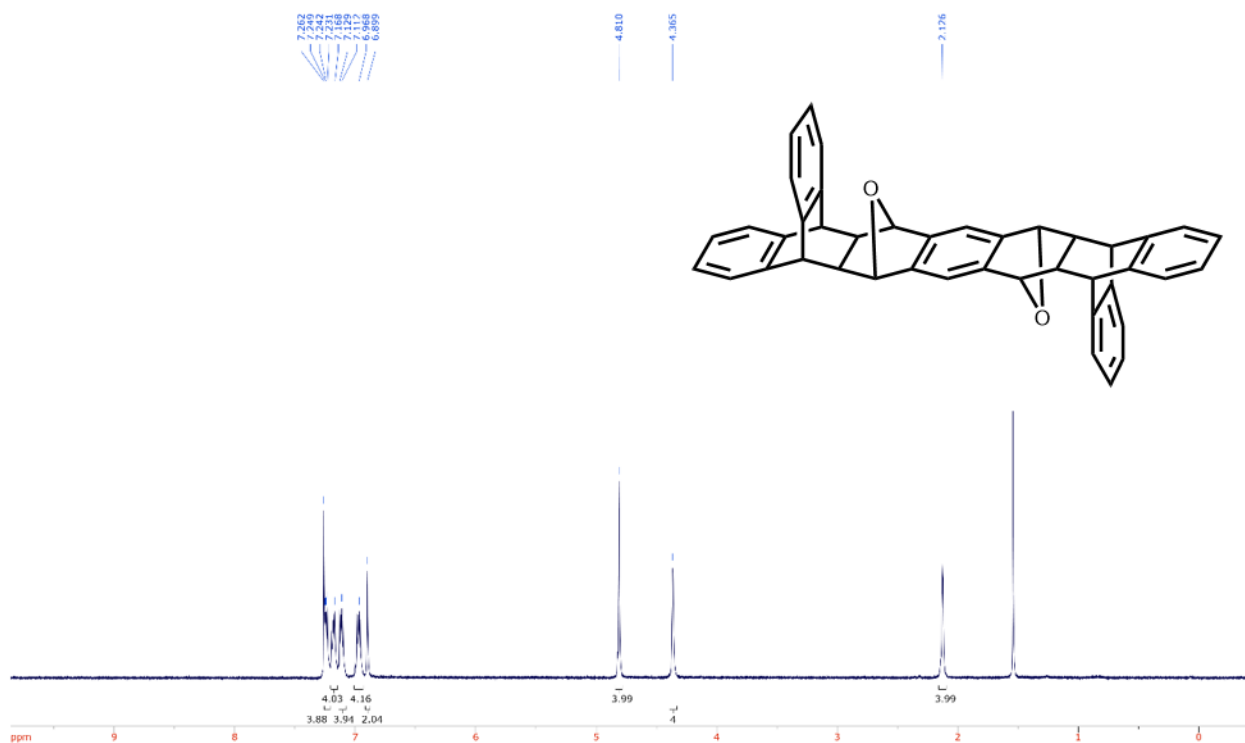
Figure A.7: ^{1}H NMR Spectra of (7)

Procedure was followed according to literature.[120] Preparation from the anti-isomer provided a white powder in a 70% yield.

^{1}H-NMR (300 MHz, CDCl$_3$) δ: 7.24 ppm (m, 4H), 7.17 ppm (m, 4H), 7.12 ppm (m, 4H), 6.97 ppm (m, 4H), 6.90 ppm (s, 2H), 4.81 ppm (s, 4H), 4.37 ppm (s, 4H), 2.13 ppm (s, 4H)
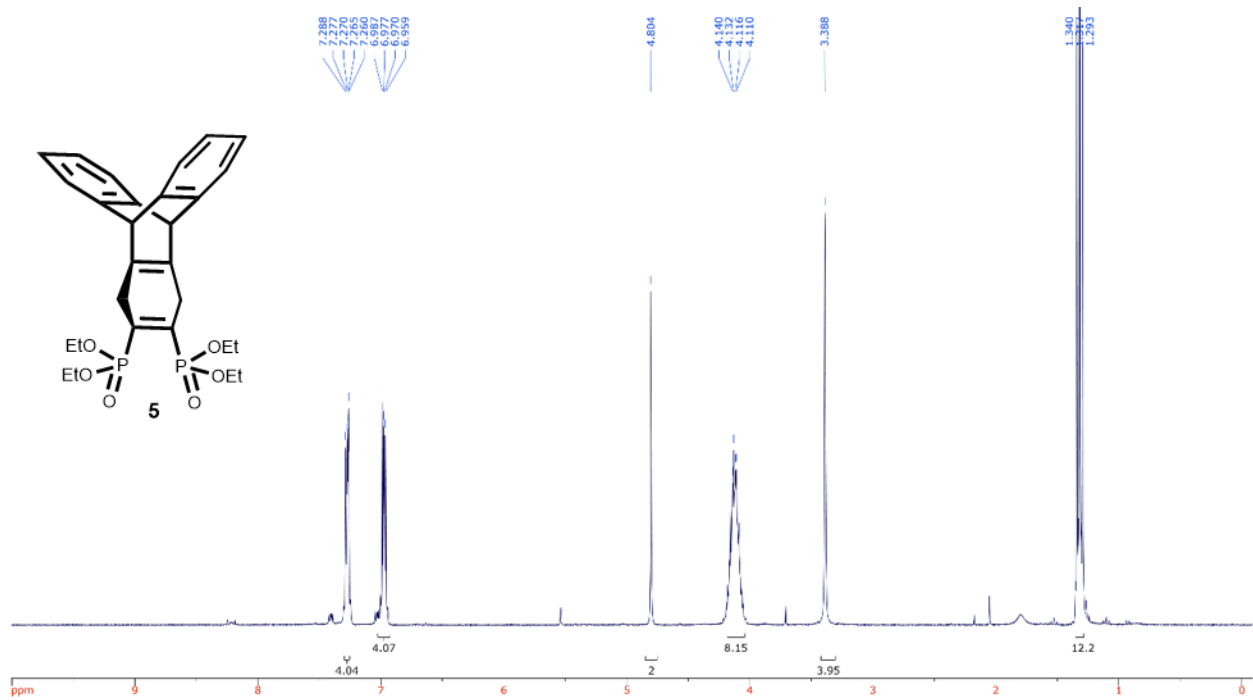
Figure A.8: ^{1}H NMR Spectra of **(8)**
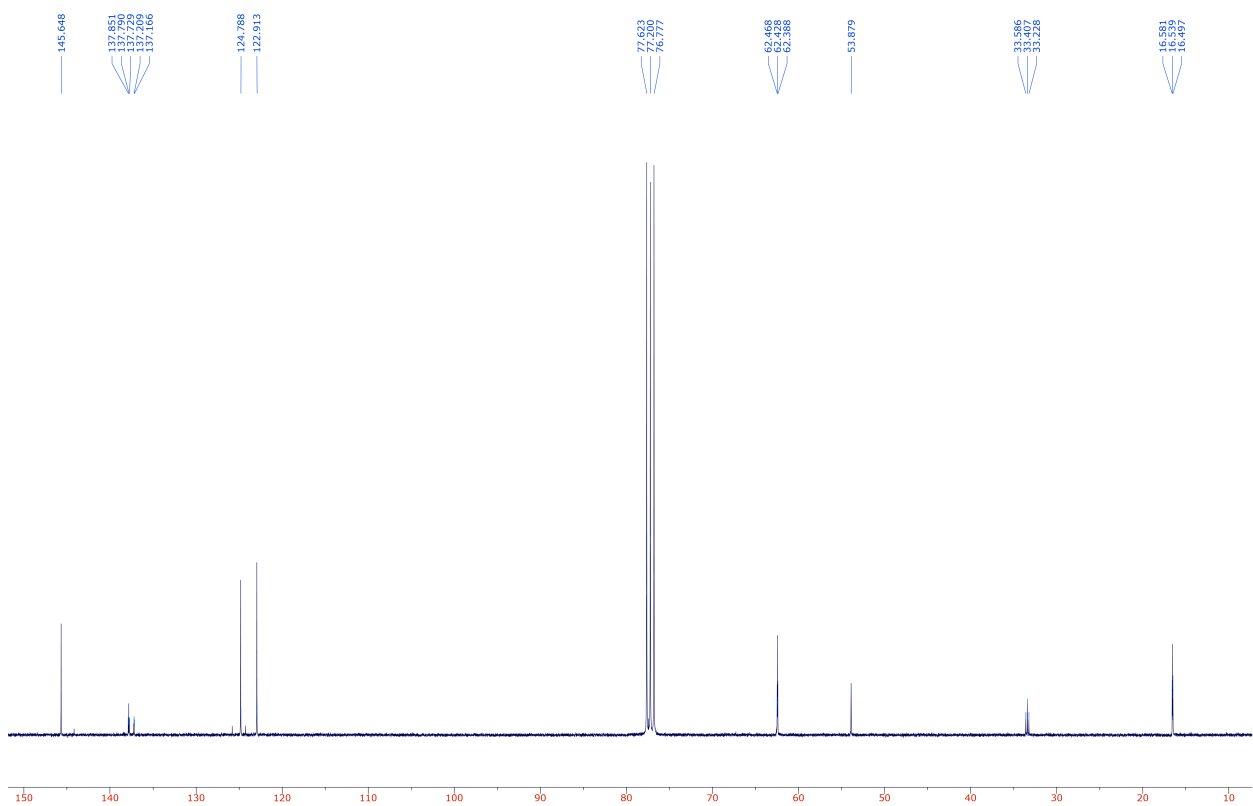
Figure A.9: ^{13}C NMR Spectra of **(8)**
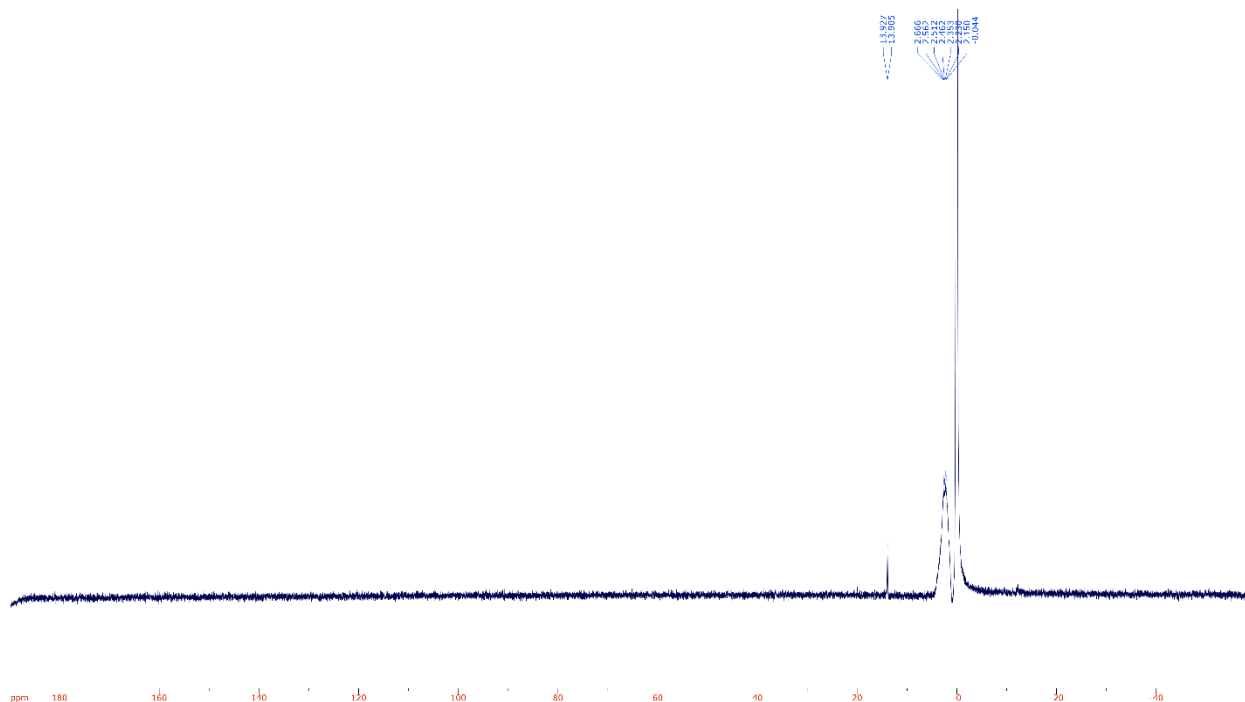
Figure A.10:^{31}P NMR Spectra of **(8)**

Bis(diethoxyphosphoryl)acetylene (130 mg, 0.434 mmol), **(2)** (100 mg, 0.434 mmol) and 4 mL of toluene were added to a 8 mL microwave tube equipped with a magnetic stir bar. The microwave tube was capped and the solution was heated with stirring at 120 °C for 24 h. The solution was purified by flash chromatography on silica gel using 90% ethyl acetate/10% methanol as the eluent system to give the product as a white solid in a 50% yield. Rf = 0.3 in 90% ethyl acetate/10% methanol. m/z (calc.) = 528.18307, m/z (found) = 528.18730.

^{1}H-NMR δ: 7.30 ppm (dd, 4H, 3.17 Hz, 5.23 Hz), 7.00 ppm (dd, 4H, 3.16 Hz, 5.27 Hz), 4.80 ppm (s, 2H), 4.12 ppm (m, 8H), 3.88 ppm (s, 4H), 1.34 ppm (t, 12H, 7.07 Hz)

^{13}C-NMR δ: 145.6 ppm, 137.8 ppm (t, 4.60 Hz), 137.2 ppm (d, 3.25 Hz), 124.7 ppm, 122.9 ppm, 62.4 ppm (t, 3.00 Hz), 53.6 ppm, 33.4 ppm (t, 13.51 Hz), 16.5 ppm (t, 3.18 Hz)

^{31}P-NMR δ: 13.9 ppm (d, 3.33 Hz)

61
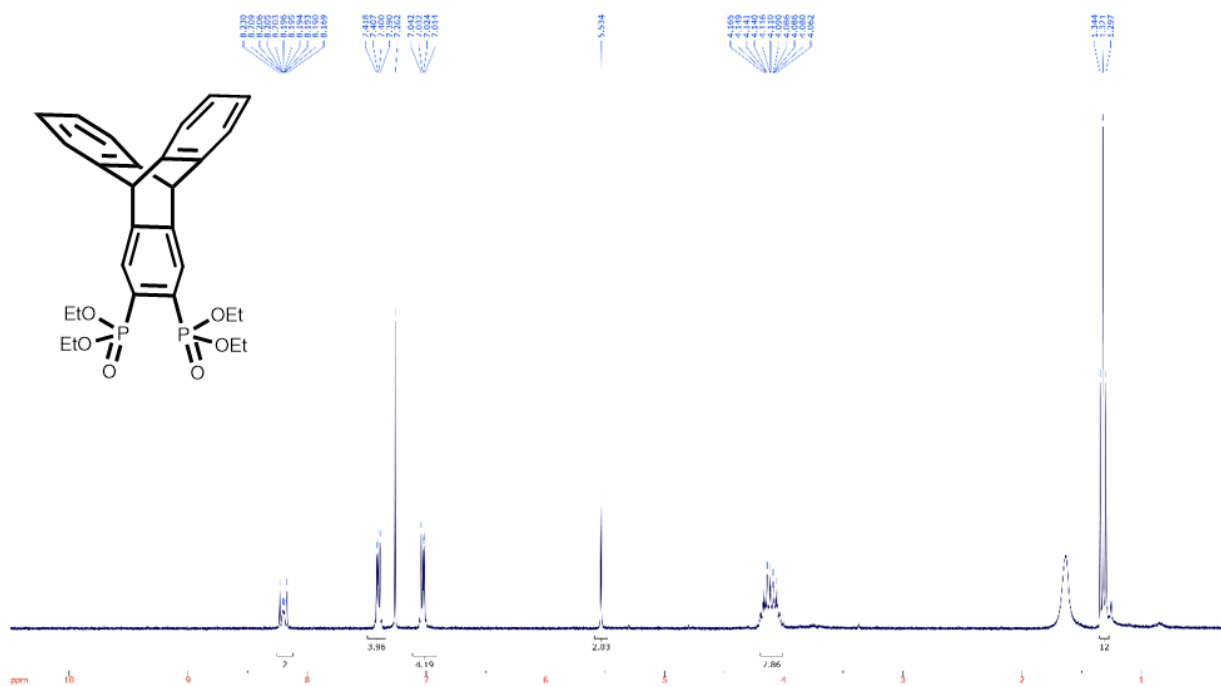
Figure A.11: ^{1}H NMR Spectra of **(9)**
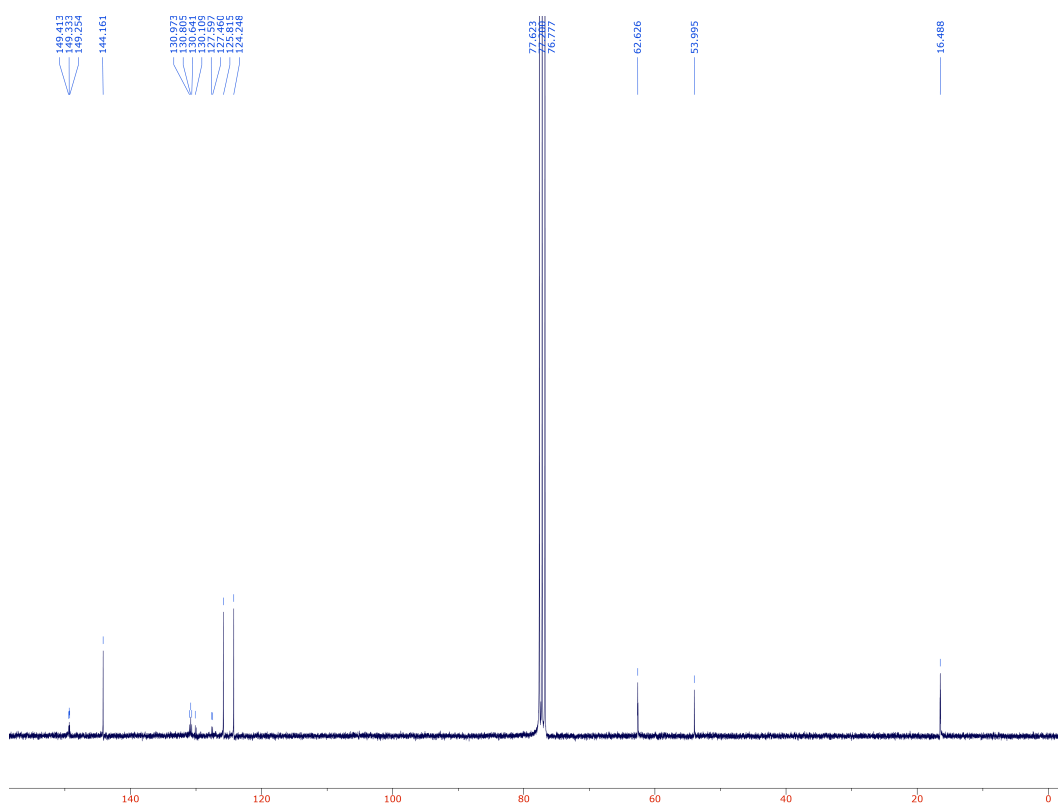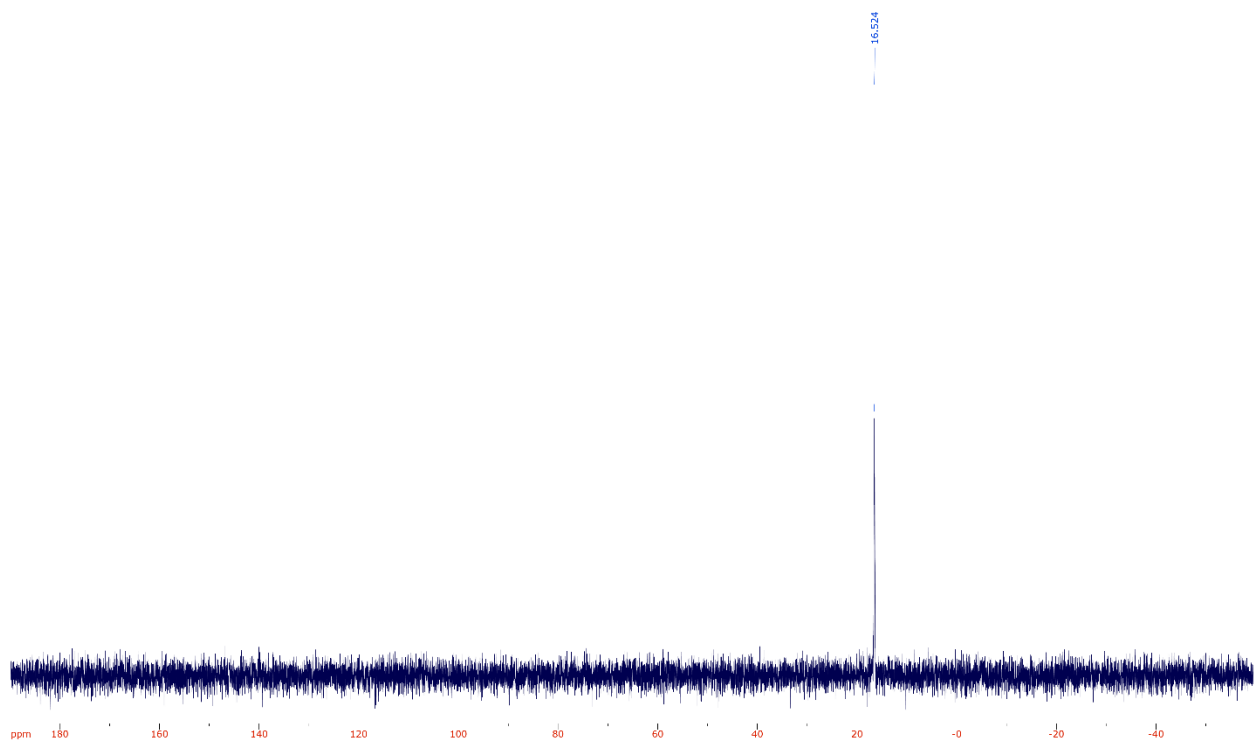
Figure A.12: ^{13}C NMR Spectra of **(9)**

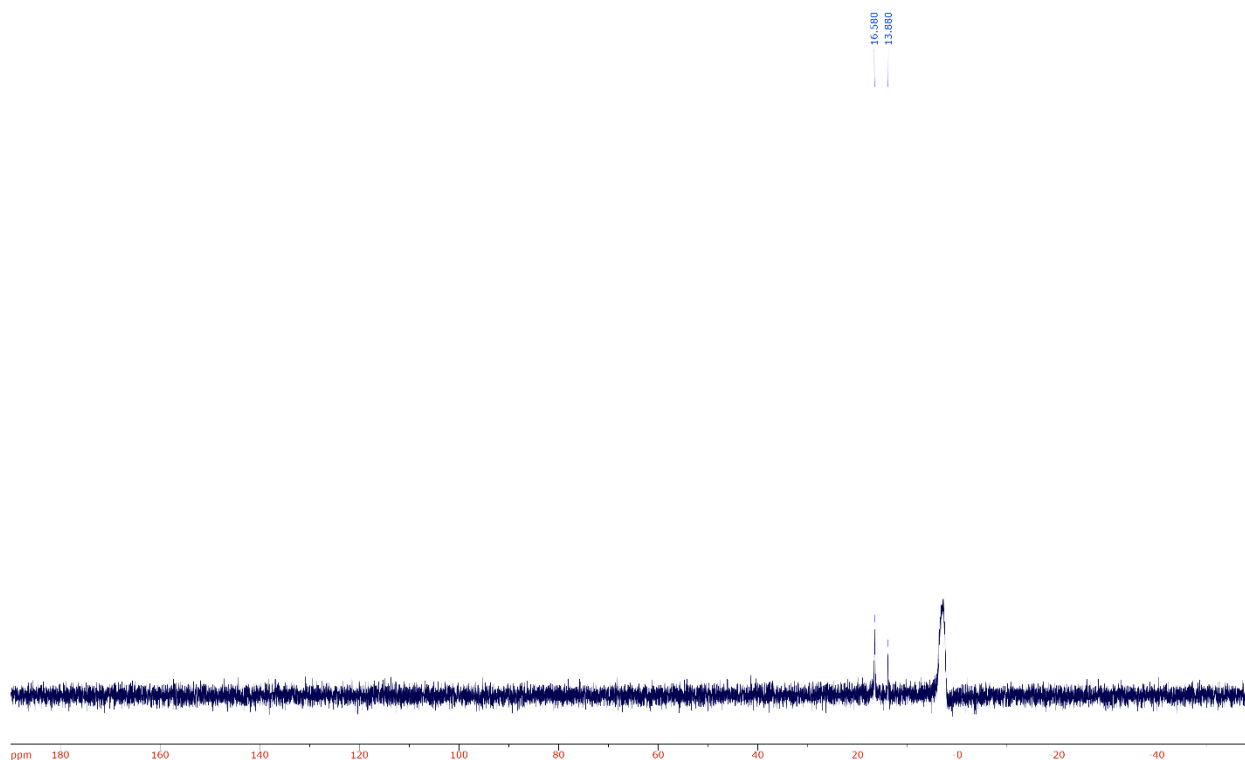Figure A.13:^{31}P NMR Spectra of **(9)**

Figure A.14:^{31}P NMR Spectra of **(9)**

2,3-Dichloro-5,6-dicyano-1,4-benzoquinone (DDQ) (118 mg, 0.520 mmol) and **(5)** (250 mg, 0.473 mmol) and 4 mL of 1,4-dioxane were added to a 8 mL microwave tube equipped with a magnetic stir bar. The microwave tube was capped and the solution was heated with stirring at 65 °C for 3 h. The solution was purified by flash chromatography on silica gel using 90% ethyl acetate/10% methanol as the eluent system to give the product as a white solid in an 80% yield. Rf = 0.3 in 90% ethyl acetate/10% methanol.

m/z (calc.) = 526.16742, m/z (found) = 526.16505.

^{1}H-NMR δ: 8.20 ppm (m, 2H), 7.40 ppm (dd, 4H, 3.21 Hz, 5.33 Hz), 7.03 ppm (d, 4H, 3.14 Hz, 5.41 Hz), 5.53 ppm (s, 2H), 4.12 ppm (m, 8H), 1.32 ppm (t, 12H, 7.07 Hz)

^{13}C-NMR δ: 149.3 ppm (t, 5.99 Hz), 144.2 ppm, 130.8 ppm (t, 12.53 Hz), 130.1 ppm, 127.5 ppm (d, 10.36 Hz), 125.8 ppm, 124.2 ppm, 62.7 ppm (t, 2.90 Hz), 54.0 ppm, 16.5 ppm (t, 3.21 Hz)

^{31}P-NMR δ: 16.5 ppm (Note: The phosphoric acid internal standard seems to be very reactive with the product and degrades upon exposure, hence two spectra are included: one by itself, and one that has **(5)** mixed in. By comparing the ^{31}P spectra with the one pertaining to **(5)**, we can deduce that the peak at 16.5 ppm does indeed belong to **(6)**.
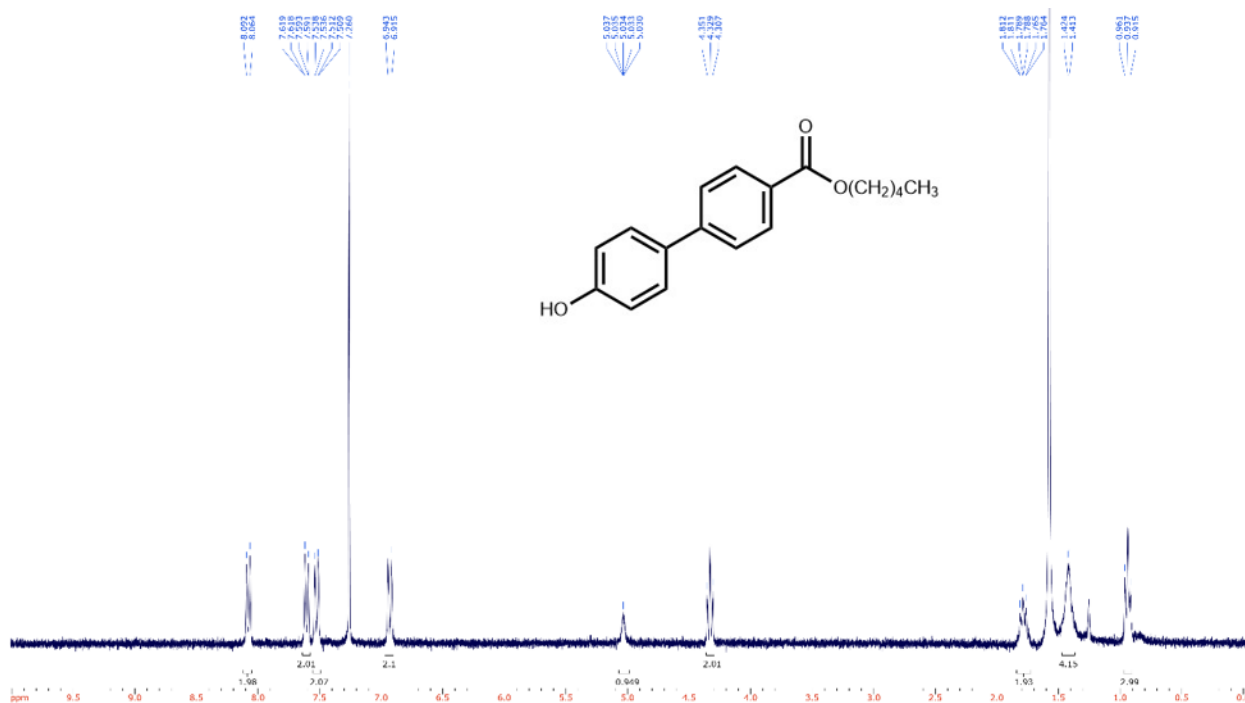

Figure A.15: ^{1}H NMR Spectra of **(10)**

Procedure was followed according to literature.[135] A yellow solid was obtained in a 48% yield.

^{1}H-NMR (300 MHz, CDCl$_3$) δ: 8.08 ppm (d, 2H, 8.66 Hz), 7.60 ppm (d, 2H, 7.99 Hz), 7.52 ppm (d, 2H, 7.96 Hz), 6.93 ppm (d, 2H, 8.45 Hz), 5.03 ppm (m, 1H), 4.32 ppm (t, 2H, 6.70 Hz), 1.78 ppm (m, 2H), 1.41 ppm (m, 4H), 0.94 ppm (t, 3H, 6.85 Hz)
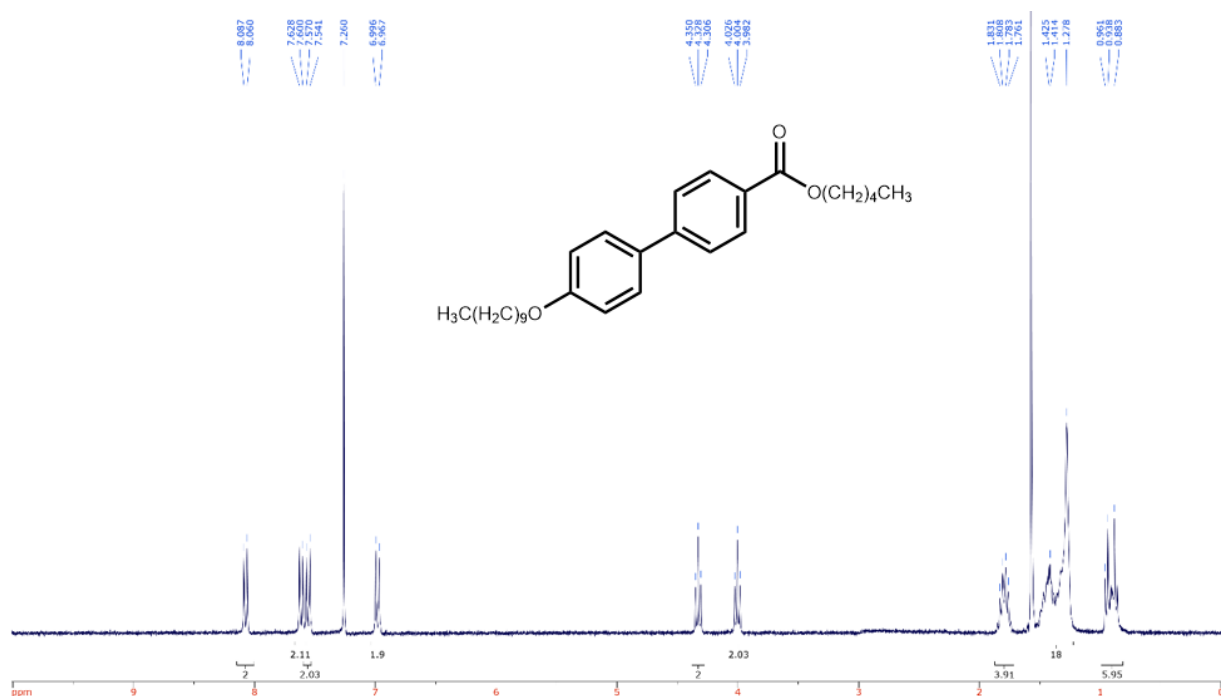
Figure A.16: ^{1}H NMR Spectra of **(11)**

Procedure was followed according to literature replacing n-iodopentane with n-bromodecane and NaH with KO^{t}Bu.[135] A yellow solid was obtained in a 88% yield.

^{1}H-NMR (300 MHz, CDCl$_3$) δ: 8.07 ppm (d, 2H, 8.25 Hz), 7.61 ppm (d, 2H, 8.34 Hz), 7.55 ppm (d, 2H, 8.65 Hz), 6.99 ppm (d, 2H, 8.71 Hz), 4.33 ppm (t, 2H, 6.68 Hz), 4.00 ppm (t, 2H, 6.51 Hz), 1.80 ppm (m, 4H), 1.35 ppm (m, 18H), 0.93 ppm (m, 6H)

A.2 Polarized Optical Microscopy

The following materials were purchased from the supplier in brackets: Plugable USB Microscope (Amazon), Polarized Lens Filters (Movie Theatre), Breadboard Electronics Kit (Amazon), Scrap Wood, Battery Holder (Digikey), 10 kΩ Resistor Digikey, Aluminum Block (University Machine Shop), Heat Resistant Polarized Light Filters (Amazon), Silicon Heating Station (Jiangyin Mengyou Electronic Heating Appliances Co., Ltd. – Alibaba), 15 kΩ Potentiometer, Digikey, 1.90" x 0.95" x 0.5" N52 Rare Earth Magnets (KJ Magnetics, Inc), Model D256A Polyimide Alignment Layers (Instec)
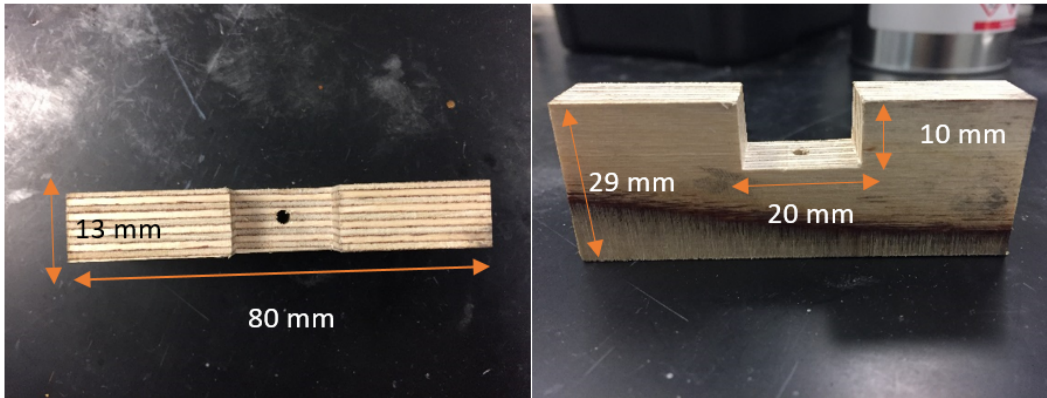
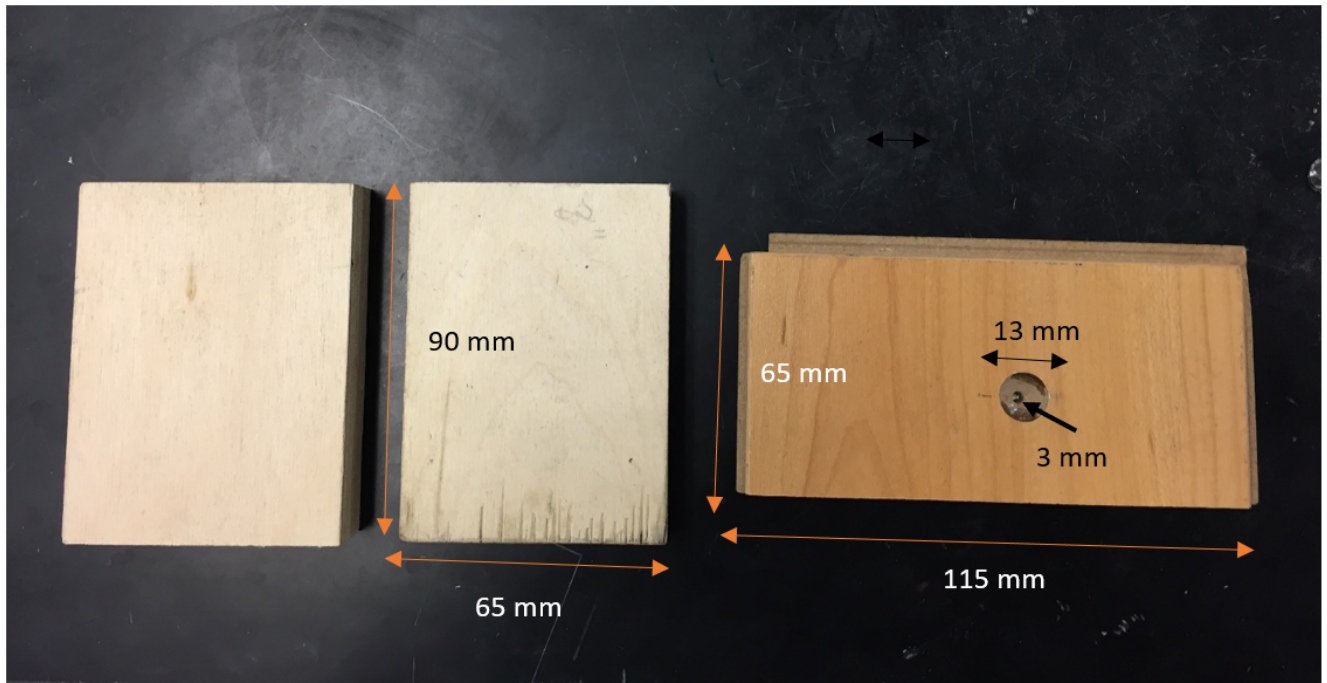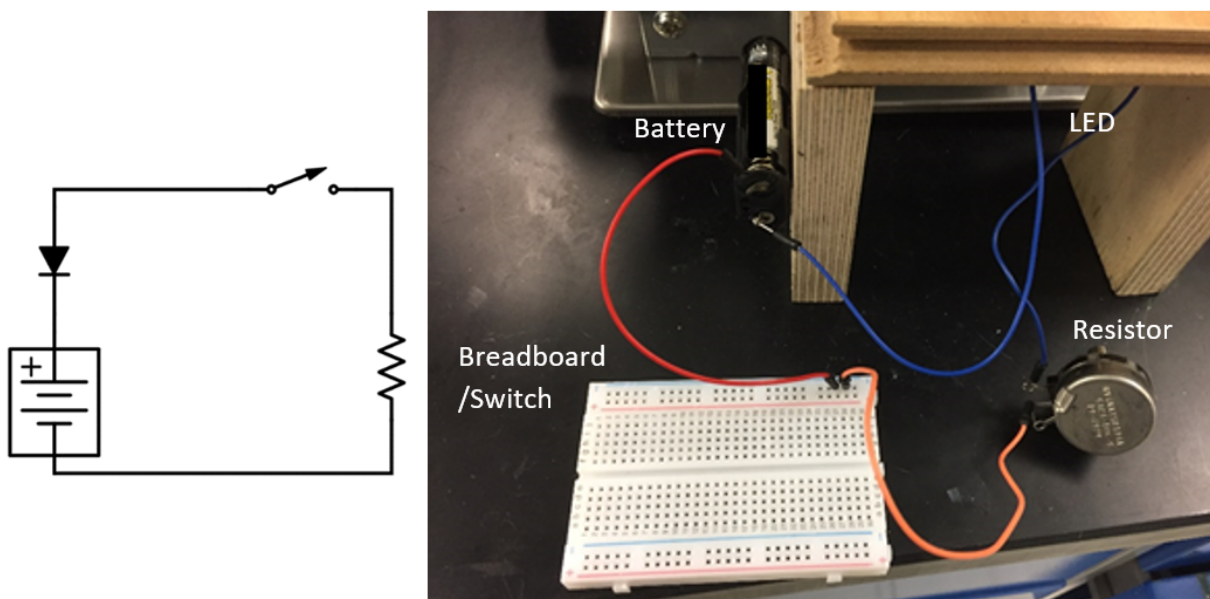Figure A.17: Dimensions of stage used for POM analysis

Figure A.18: Dimensions of POM housing

S5: Wiring schematic for the setup and a blown up view of actual wiring

Figure A.19: POM Circuitry

Upon completion, a thin film of liquid crystal was deposited on glass in a similar manner as found in the functionalization procedure. The samples were put into the magnetic alignment apparatus at room temperature, allowed to equilibrate and imaged directly.

A.3 Construction of the Magnetic Alignment Apparatus

The platforms were milled out of aluminum initially as a rectangular block in the following dimensions: 1 cm x 8 cm x 4 cm for the 0.6 T design and 0.5 mm x 8 cm x 4 cm for the 0.9 T design. In both blocks, cutouts with dimensions 4 cm x 1 cm were removed from the centre. Two holes were drilled out: one in the centre of the block using a 2 mm drill bit so that polarized optical microscopy could be performed, the other on the side using a 3 mm drill bit for space to insert a thermometer. The resulting platforms were each sandwiched between four N52 magnets of dimensions 1 1/2" x 3/4" x 3/4" (KJ Magnetics, USA) to yield the final apparatus. Magnetic field readings were performed using a Gaussmeter

Model GM2 paired with the standard 0-30 Kilogauss probe attachment (AlphaLab, USA). The measurement was taken with the probe lying flat on the surface of one of the magnets exposed in the pocket.
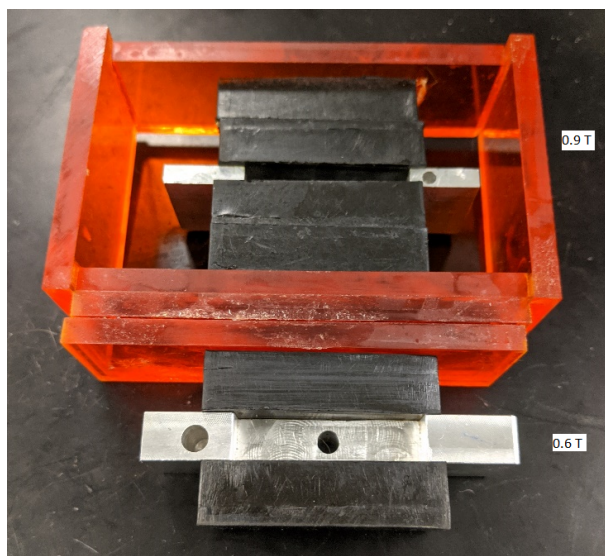

Figure A.20: Conjoined 0.9 T and 0.6 T magnetic alignment apparatus

A.4 Raman Spectroscopy

Characteristic nanotube stretches in the radial breathing region were found using laser light (533 nm, green 25% laser filtering) with a He-Ne laser using a Horiba Jabin Yvon HR800 Raman spectrometer with Olympus BX41 Microscope in the backscattering configuration, with a spectral resolution of 0.3 cm^{-1}. All measurements were performed at room temperature in ambient atmosphere with a laser power of 1 mW and spectra were recorded with an exposure time of 5 s and summed over 5 accumulations. Mapping was performed over a 30 μm x 30 μm with a step size of 1.6 μm (x and y). The beam was focused on the samples with a 20x microscope objective and a numerical aperture of 0.4. The minimum power for which a signal could be measured was limited by the signal to noise resolution of the detector in the spectrometer. Non-weighted Lorentzian modelling was used to process all spectral data followed by smoothing with a Savitzky-Golay filter. All processing and visualization of data were performed on Python v3.6 using the matplotlib library.

CNT folds/chiralities were determined through Kataura plot analysis. The reference plots generated (Figure A.1) contain the following parameters: γ_o= 2.9 eV, C-C bond length = 0.144 nm, and ω_{RBM}= 248/d_{CNT}. Full mapping of the CNT's can be found on the Maruyama group website.[136]
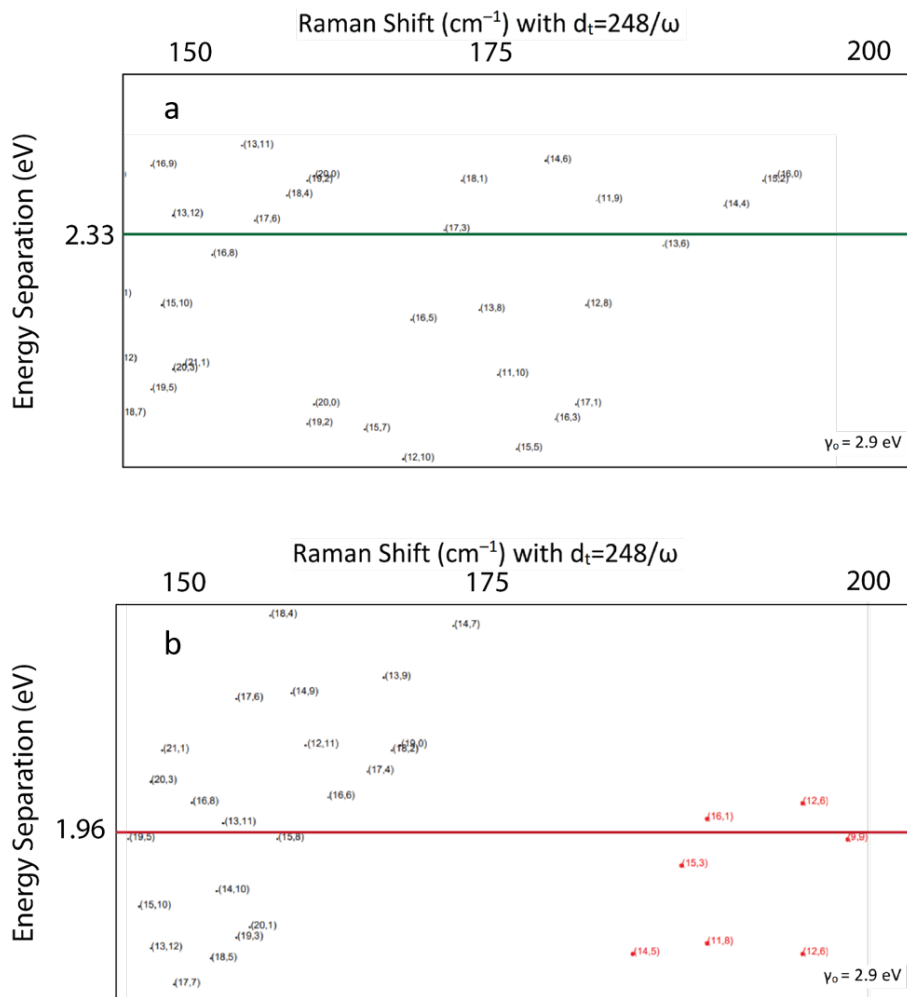

Figure A.21: a) Kataura map of CNT's close in resonance energy to 2.33 eV laser b) Kataura map of CNT's close in resonance energy to 1.96 eV laser

A.5   Functionalization via Alignment Layer

10 mm x 5 mm silicon (100) (Pure Wafer, USA) shards were treated with a steady stream of hydrogen plasma at a rate of 100 sccm for 15 minutes on an LFC 150 G (Samco, Liechtenstein).5 μL of the liquid crystal mixture comprising of an iptycene molecule (1.3 mol%) dissolved in liquid crystal was pressed between the polished side of a shard of silicon and a planar polyimide alignment layer rubbed along the x-(long) direction of an indium tin oxide surface (Instec Inc, USA). The sample was left in an oven set to 75 °C for one day (for liquid crystal (**4**)) and room temperature for two days (for iptycene (**6**)). The substrate wafer was removed from the alignment layer, rinsed with HPLC grade dichloromethane (Millipore-Sigma, CA) and dried with N_2. The functionalized silicon surfaces were placed polished side up in 10 mL of 90% pure sc-SWNTs solution (1 mg/100 mL) (NanoIntegris Technologies Inc, CA) for 48 hours. The SWNTs solution was sonicated before the sample was put in to avoid nanotube agglomeration – making for a homogenous solution. Samples were rinsed with Milli-Q water and dried with N_2, and their surface was analyzed with AFM and Raman spectroscopy.

A.6   Functionalization via Magnetic Fields

10 mm x 5 mm silicon (100) (Pure Wafer, USA) shards were treated with a steady stream of hydrogen plasma at a rate of 100 sccm for 15 minutes on an LFC 150 G (Samco, Liechtenstein). 5 μL of the liquid crystal mixture comprising of iptycene (**1**) (1.3 mol%) dissolved in 8-CB (Millipore-Sigma, CA) was pressed between two shards of silicon. The top shard was slowly peeled from the bottom shard and immediately placed in the magnetic alignment apparatus. The apparatus was placed in a room set to 20 °C for two days. The substrate wafer was removed from the alignment layer, rinsed with HPLC grade dichloromethane (Millipore-Sigma, CA) and dried with N_2. The functionalized silicon surfaces were placed polished side up in 10 mL of 90% pure sc-SWNTs solution (1 mg/100 mL) (NanoIntegris Technologies Inc, CA) for 48 hours. The SWNTs solution was sonicated before interacting with the sample to avoid CNT agglomeration. Samples were rinsed with Milli-Q water and dried with N_2, and their surface was analyzed with AFM and Raman spectroscopy. The drop-cast sample was prepared by placing one drop of homogeneous 90% sc-SWNT's solution onto a glass substrate pre-cleaned with pirahna solution and left to dry in the fume hood.

A.7   Images

Figure A.22: Polarized optical microscope images of 8-CB mixture in 0.6 T environment (left) and 0.9 T environment (right). Mild imperfections can be seen on the left as dots. Darker image on the right arises from a rotated stage to spot any imperfections; none were spotted
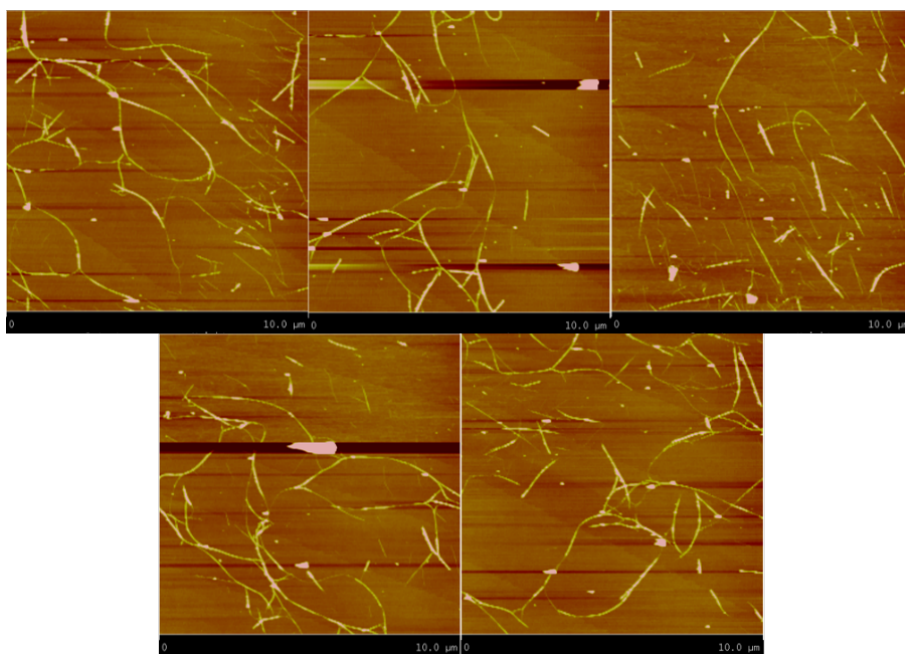

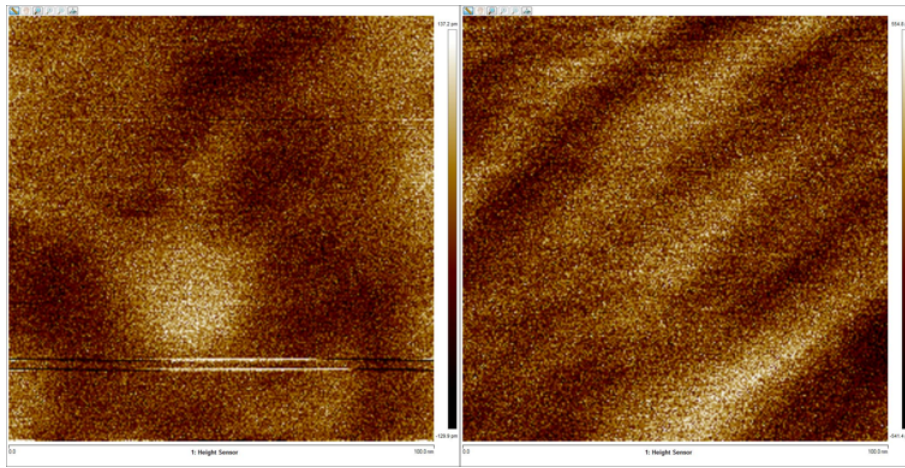Figure A.23: Full set of AFM images from analysis on ZLI-1185 ART trials

Figure A.24: Representative images from ART trials with liquid crystal **(11)**
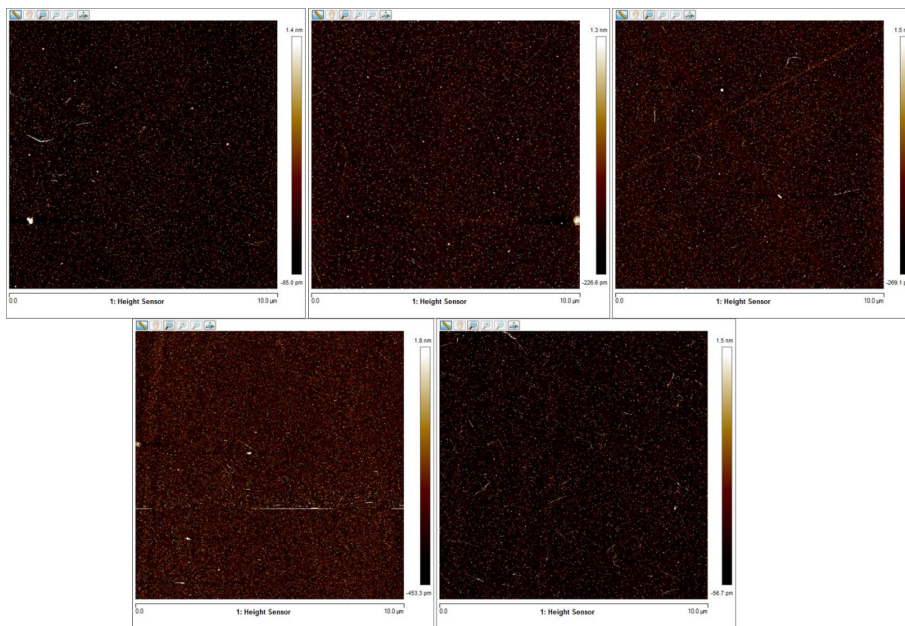

Figure A.25: Full set of AFM images from analysis on 0.6 T modified ART trials
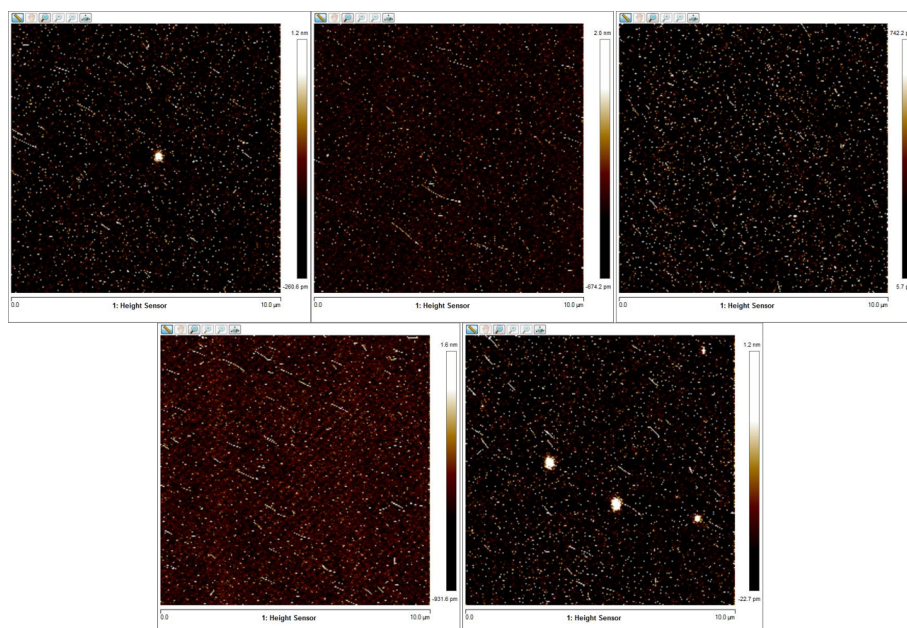
Figure A.26: Full set of AFM images from analysis on 0.9 T modified ART trials. White spots are artifacts as a result of an unknown interference with the probe tip
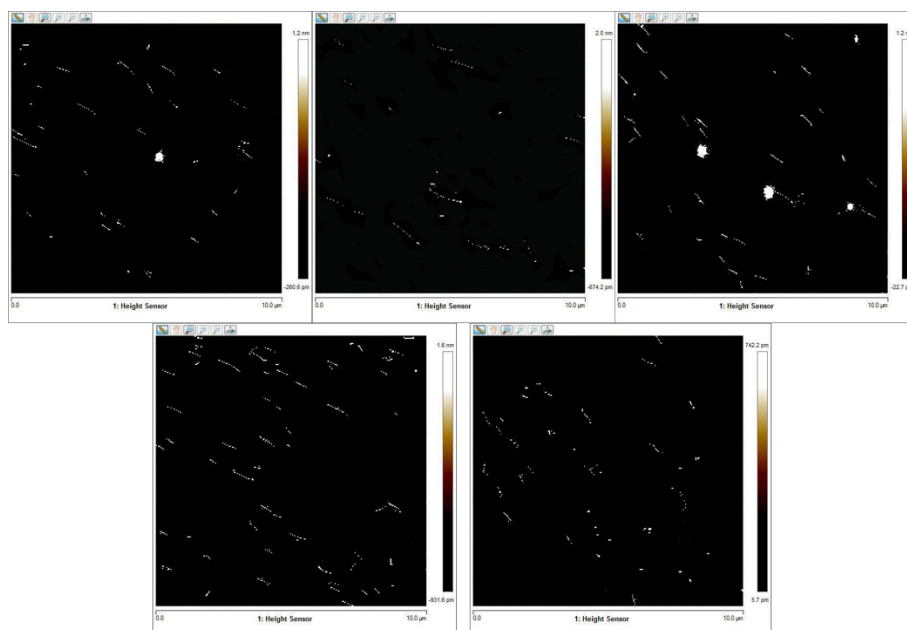

Figure A.26: Full set of modified AFM images from analysis on 0.9 T modified ART trials. White noise artifacts from the AFM were removed during this retouch while

maintaining all the features on the surface

A.8   Image Retouching

Editing was performed on Adobe Photoshop CS6 with the following conditions:

Filter -100 Saturation +300 Contrast Erase any points that are not clusters of 3+ "Color Range" 200 Fuzziness Select the clusters and expand by 1 pixel Use selection on original to select point Colorize at 25 saturation

+500 Contrast +300 Brightness "Color Range" 200 Fuzziness Select the clusters and expand by 1 pixel Use selection on original to select point Colorize at 25 saturation -50 to Lightness